Atmospheric
Chemistry
and Physics
Discussions

1 Aerosol distribution in the northern Gulf of Guinea: local anthropogenic

2 sources, long-range transport and the role of coastal shallow

3 circulations

4

5 Cyrille Flamant[1], Adrien Deroubaix[1,2], Patrick Chazette[3], Joel Brito[4], Marco Gaetani[1],

6 Peter Knippertz[5], Andreas H. Fink[5], Gaëlle de Coetlogon[1], Laurent Menut[2], Aurélie

7 Colomb[4], Cyrielle Denjean[6], Remi Meynadier[1], Philip Rosenberg[7], Regis Dupuy[4], Alfons

8 Schwarzenboeck[4] and Julien Totems[3]

9

10 [1]Laboratoire Atmosphères Milieux Observations Spatiales, Sorbonne Université,

11 Université Paris-Saclay and CNRS, Paris, France

12 [2]Laboratoire de Météorologie Dynamique, Ecole Polytechnique, IPSL Research

13 University, Ecole Normale Supérieure, Université Paris-Saclay, Sorbonne Université,

14 CNRS, Palaiseau, France

15 [3]Laboratoire des Sciences du Climat et de l'Environnement, CEA, CNRS, Université

16 Paris-Saclay, Gif-sur-Yvette, France

17 [4]Laboratoire de Météorologie Physique, Université Clermont Auvergne, CNRS,

18 Clermont-Ferrand, France

19 [5]Institute of Meteorology and Climate Research, Karlsruhe Institute of Technology,

20 Karlsruhe, Germany

21 [6]Centre National de Recherches Météorologiques, Météo-France and CNRS,

22 Toulouse, France

23 [7]Institute of Climate and Atmospheric Science, School of Earth and Environment,

24 University of Leeds, Leeds, United Kingdom

25

Atmospheric
Chemistry
and Physics
Discussions

Open Access

26

Abstract

28

29 *The complex vertical distribution of aerosols over coastal southern West Africa (SWA)*

30 *is investigated using airborne observations and numerical simulations. Observations*

31 *were gathered on 2 July 2016 offshore of Ghana and Togo, during the field phase of*

32 *the Dynamics-Aerosol-Chemistry-Cloud Interactions in West Africa project. The*

33 *aerosol loading in the lower troposphere includes emissions from coastal cities*

34 *(Accra, Lomé, Cotonou and Lagos) as well as biomass burning aerosol and dust*

35 *associated with long-range transport from Central Africa and the Sahara,*

36 *respectively. Our results indicate that the aerosol distribution is impacted by*

37 *subsidence associated with zonal and meridional regional scale overturning*

38 *circulations associated with the land-sea surface temperature contrast and*

39 *orography over Ghana and Togo. Numerical tracer release experiments highlight the*

40 *dominance of aged emissions from Accra on the observed pollution plume loadings*

41 *over the ocean. The contribution of aged emission from Lomé and Cotonou is also*

42 *evident above the marine boundary layer. Lagos emissions do not play a role for the*

43 *area west of Cotonou. The tracer plume does not extend very far south over the*

44 *ocean (i.e. less than 100 km from Accra), mostly because emissions are transported*

45 *northeastward near the surface over land and westward above the marine*

46 *atmospheric boundary layer. The latter is possible due to interactions between the*

47 *monsoon flow, complex terrain and land-sea breeze systems, which support the*

48 *vertical mixing of the urban pollution. This work sheds light on the complex – and to*

49 *date undocumented – mechanisms by which coastal shallow circulations distribute*

50 *atmospheric pollutants over the densely populated SWA region.*

51

Atmospheric
Chemistry
and Physics
Discussions

52

1. Introduction

54

Aerosol-cloud-climate interactions play a fundamental role in radiative balance and energy redistribution in the tropics. Aerosol particles from natural and anthropogenic origins can serve as cloud condensation nuclei (Haywood and Boucher, 2000; Carslaw et al., 2010) and interact with solar and terrestrial radiation through absorption and scattering.

60

The atmosphere over southern West Africa (SWA) is a complex mix of local emissions (vegetation, traffic, domestic and waste fires, power plants, oil and gas rigs, ships) and remote sources (dust from the north and wild-fire related biomass burning aerosols from Central Africa) (Knippertz et al., 2015a, Brito et al., 2018). In order to enhance our understanding of aerosol-cloud-climate interactions in SWA, it is of paramount importance to better characterize the composition and vertical distribution of the aerosol load over the eastern tropical Atlantic. This is particularly vital, since SWA is currently experiencing major economic and population growths (Liousse et al., 2014), and is projected to host several megacities (cities with over 10 million inhabitants) by the middle of the 21st century (World Urbanization Prospect, 2015). This will likely boost anthropogenic emissions to unprecedented levels and imply profound impacts on population health (Lelieveld et al., 2015), on the radiative budget over SWA and also on the West African Monsoon (WAM) system (Knippertz et al., 2015b). This will also add to the dust and biomass burning aerosol related perturbations already evidenced for the precipitation in the area (e.g. Huang et al., 2009). Likewise, urban pollution may also affect surface-atmosphere interactions and associated lower tropospheric dynamics over SWA as for instance dust over the

78 tropical Atlantic (e.g. Evan et al., 2009) or biomass burning aerosols over Amazonia

79 (Zhang et al., 2008, 2009).

80

81 One of the aims of the EU-funded project Dynamics-Aerosol-Chemistry-Cloud

82 Interactions in West Africa (DACCIWA, Knippertz et al., 2015b) is to understand the

83 influence of atmospheric dynamics on the spatial distribution of both anthropogenic

84 and natural aerosols over SWA. One particularly important aspect is the fate of

85 anthropogenic aerosols emitted at the coast as they are being transported away

86 from the source. In addition, DACCIWA aims at assessing the impact of this complex

87 atmospheric composition on the health of humans and ecosystems.

88

89 Urban aerosols are mostly transported with the southwesterly monsoon flow below

90 700 hPa (e.g. Deroubaix et al., 2018). They may also reach the nearby ocean as the

91 result of complex dynamical interactions between the monsoon flow, the

92 northeasterly flow from the Sahel above and the interactions with the atmospheric

93 boundary layer (ABL) over the continent coupling the two layers when it is fully

94 developed during daytime. This is because, as opposed to the marine ABL, the

95 continental ABL exhibits a strong diurnal cycle (e.g. Parker et al., 2005; Lothon et al.,

96 2008; Kalthoff et al., 2018). On hot, cloud-free summer days, land-sea breeze systems

97 can develop at the coast (in conditions of moderate background monsoon flow,

98 Parker et al., 2017), which contribute to the transport of pollutants emitted along the

99 urbanized coastal strip of SWA.

100

101 The main objective of the present study is to understand how the lower tropospheric

102 circulation over SWA shapes the urban pollution plume emitted from coastal cities

103 such as Accra, Lomé, Cotonou and Lagos, both over the Gulf of Guinea and inland.

Atmospheric
Chemistry
and Physics
Discussions

104   Here, we take advantage of the airborne measurements acquired during the

105   DACCIWA field campaign (June–July 2016, Flamant et al., 2018) as part of the

106   European Facility for Airborne Research (EUFAR) funded Observing the Low-level

107   Atmospheric Circulation in the Tropical Atlantic (OLACTA) project to assess the

108   characteristics of different aerosol layers observed over the Gulf of Guinea. To study

109   the role of atmospheric dynamics on aerosol spatial distribution, we use a unique

110   combination of airborne observations from the 2 July 2016, space-borne observations

111   and finally high-resolution simulations performed using the Weather and Research

112   Forecast (WRF) and CHIMERE models.

113

114   The airborne and space-borne data used in this paper are presented in Section 2,

115   whereas the simulations are detailed in Section 3. Section 4 presents the synoptic

116   situation and airborne operations over SWA on 2 July 2016. Atmospheric composition

117   over the Gulf of Guinea as observed from aircraft in situ and remote sensing data is

118   discussed in Section 5. Insights into the distribution of anthropogenic aerosols from

119   tracer experiments are presented in Section 6 and long-range transport of aerosols

120   related to regional-scale dynamics is described in Section 7. The influence of lower-

121   tropospheric overturning circulations induced by the land-sea surface temperature

122   gradient on the vertical distribution of aerosols over SWA is discussed in Section 8. In

123   Section 9, we summarize and conclude.

124

125   2. Data

126

127   2.1 Airborne observations

128

129   During the DACCIWA field campaign, airborne operations on the afternoon of 2 July

130   2016 were conducted with the ATR 42 of the Service des Avions Français Instrumentés

131   pour la Recherche en Environnement (SAFIRE) over the Gulf of Guinea (**Figure 1**). The

132   afternoon flight was carried out in the framework of the EUFAR OLACTA project

133   (Flamant et al., 2018). The aircraft was equipped with in situ dynamical and

134   thermodynamical probes (yielding mean and turbulent variables), as well as in situ

135   aerosol and cloud probes, and gas phase chemistry instruments. It also carried

136   several radiometers (upward and downward looking pyranometers and

137   pyrgeometers) as well as the Ultraviolet Lidar for Canopy Experiment (ULICE, Shang

138   and Chazette, 2014). **Table 1** summarizes the instruments used in this study (see the

139   Supplement of Flamant et al., 2018 for the complete ATR 42 payload during the field

140   campaign).

141

142   2.1.1 ULICE observations

143

144   The ULICE system was specifically designed to monitor the aerosol distribution in the

145   lower troposphere. During the DACCIWA field campaign, ULICE was pointing to the

146   nadir. The system's nominal temporal and along-line-of-sight resolutions are 100 Hz

147   and 15 m, respectively. In the present study, we use lidar-derived profiles of aerosol-

148   related properties averaged over 1000 laser shots (~10 s sampling).

149

150   The ULICE receiver implements two channels for the detection of the elastic

151   backscatter from the atmosphere in the parallel and perpendicular polarization

152   planes relative to the linear polarization of the emitted light. The design and the

153   calculations to retrieve the depolarization properties are explained in Chazette et al.

154   (2012). Using co- and cross-polarization channels, the lidar allows identifying non-

155   spherical particles in the atmosphere such as dust. The overlap factor is nearly

156   identical for the two polarized channels, thereby permitting the assessment of the

157   volume depolarization ratio (VDR) very close to the aircraft (~150 m).

158

159   Lidar-derived extinction coefficient profiles (as well as other optical properties) are

160   generally retrieved from so-called inversion procedures as abundantly described in

161   the literature (e.g. Chazette et al., 2012). During the DACCIWA field campaign the

162   lack of adequate observations did not allow us to perform proper retrievals of

163   aerosol optical properties using such procedures. Hence, in the following we only use

164   the apparent scattering ratio (ASR, the ratio of the total apparent backscatter

165   coefficient to the molecular apparent backscatter coefficient denoted R_{app}) and

166   the VDR. Details are given in **Appendix A**, together with the characteristics of the

167   lidar system.

168

169   Generally speaking, the VDR values observed during the flight are not very high and

170   absolute values may be subject to biases. Nevertheless, relative fluctuations of VDR

171   are accurately measured and useful as indicators of changes in aerosol properties.

172

173   2.1.2 Aerosol and gas phase chemistry measurements

174

175   For this study, we focus on available observations that can provide insights into the

176   origin of the aerosol distribution over coastal SWA, namely biomass burning aerosols,

177   dust and urban pollution:

178   -   **Biomass burning aerosols**: identification was conducted at times of enhanced

179   ozone (O_3) and carbon monoxide (CO) mixing ratios as well as aerosol

180   parameters such as light absorption/extinction and number concentration.

Atmospheric
Chemistry
and Physics
Discussions

181   -   **Urban pollution**: the main tracers used were CO, nitrogen oxide (NOx) and

182   total (>10 nm) particle number concentrations;

183   -   **Terrigenous aerosols (dust)**: layers were identified at times of enhanced

184   aerosol parameters (particularly super micron aerosols), in complement to the

185   lidar-derived VDR observations and not followed by CO or O_3 enhancements

186   (mostly associated with biomass burning here).

187

188   In addition, absorption Angstrom exponent (AAE) measurements are used to

189   distinguish urban air pollution from biomass burning smoke (Clarke et al., 2007) and

190   mineral dust (Collaud Coen et al., 2004). In general the AAE values for carbonaceous

191   particles are ~1 for urban pollution, between 1.5 and 2 for biomass smoke and

192   around 3 for dust (Bergstrom et al., 2007).

193

194   The Particle Soot Absorption Photometer (PSAP, model PSAP3L) measures the aerosol

195   optical absorption coefficient at three wavelengths (467, 530 and 660 nm) with a

196   sampling time of 10 s. The data were corrected for multiple scattering and

197   shadowing effects according to Bond et al. (1999) and Müller et al. (2009). Data with

198   filter transmission under 0.7 are removed as corrections are not applicable.

199   Furthermore, PSAP measurements were used to compute the AAE. The particle

200   extinction coefficient is measured with a cavity attenuated phase shift particle light

201   extinction monitor (CAPS-PMex, Aerodyne Research) operated at the wavelength of

202   530 nm. Data were processed with a time resolution of 1 s. An integrated

203   nephelometer (Ecotech, model Aurora 3000) provided aerosol light scattering at

204   three wavelenghts (450, 550 and 700 nm), which was used to correct for the impact

205   of aerosol scattering based on the correction scheme by Anderson and Ogren

206   (1998) and using correction factors obtained by Müller et al. (2011) without a

207   submicron size cut-off. The nephelometer was calibrated with particle-free air and

208   high-purity CO_2 prior to and after the campaign.

209

210   Prior to the campaign, the CAPS data were evaluated against the combination of

211   the nephelometer and the PSAP measurements. The instrument intercomparison has

212   been performed with purely scattering ammonium sulfate particles and with strongly

213   absorbing black carbon particles. Both types of aerosols were generated by

214   nebulizing a solution of the respective substances and size-selected using a

215   Differential Mobility Analyzer. For instrument intercomparison purposes, the extinction

216   coefficient from the nephelometer and PSAP was adjusted to that for 530 nm by

217   using the scattering and absorption Angstrom exponent. The instrument evaluation

218   showed an excellent accuracy of the CAPS measurements by comparison to the

219   combination of nephelometer and PSAP measurements. The level of uncertainty

220   obtained for the test aerosol was beyond the upper limit of the CAPS uncertainty

221   which was estimated to be +-3% according to Massoli et al. (2010).

222

223   Total particle concentration for particle diameters above 10 nm (N_{10}) are made using

224   a Condensational Particle Counter (CPC, model MARIE built by University of Mainz),

225   calibrated prior to the experiment (sampling time 1 Hz). Aerosol optical size in the

226   range 0.25–25 µm is measured using an Optical Particle Counter (OPC, model 1.109

227   from GRIMM Technologies) in 32 channels, with a 6 s sampling rate. Particulate

228   matter number concentrations for size ranges smaller than 1 µm, between 1 and 2.5

229   µm and between 2.5 and 10 µm are computed from the OPC, and are referred to

230   N_{PM1}, $N_{PM2.5}$ and N_{PM10} respectively, in the following. The GRIMM OPC was calibrated

231   with size-standard particles prior and after the field campaign.

232

Atmospheric
Chemistry
and Physics
Discussions
Open Access
EGU

233   Sampling with all the above mentioned instruments is achieved through the

234   Community Aerosol Inlet of the ATR 42.

235

236   Regarding gas phase chemistry, we make use of an O_3 analyzer and a NOx analyzer

237   from Thermo Environmental Instruments (TEI Model 49 and TEI 42CTL, respectively).

238   Carbon monoxide (CO) measurements are performed using the near-infrared cavity

239   ring-down spectroscopy technique (G2401, Picarro Inc., Santa Clara, CA, USA), with

240   a time resolution of 5 s.

241

242   All in-cloud measurements are removed from the data shown here.

243

244   2.2 Space-borne observations

245

246   The Spinning Enhanced Visible and Infra-Red Imager (SEVIRI), onboard Meteosat

247   Second Generation (MSG), measures aerosol optical depth (AOD) with spatial and

248   temporal resolutions of 10 km and 15 min, respectively (Bennouna et al., 2009). We

249   use the operational version 1.04 of the AOD product at 550 nm, downloaded from

250   the ICARE data service center (http://www.icare.univ-lille1.fr/).

251

252   The Moderate Resolution Imaging Spectroradiometer (MODIS, Salmonson et al., 1989;

253   King et al., 1992) flies aboard the polar-orbiting platforms Aqua and Terra. Terra

254   crosses the Equator from north to south in the morning (~1030 local time), whereas

255   Aqua crosses from south to north during the afternoon (~1330 local time). They

256   provide a complete coverage of the Earth surface in one to two days with a

257   resolution between 250 and 1000 m, depending on the spectral band. In the

258   following, we use MODIS-derived level 2 AODs at 550 nm from both Terra and Aqua.

Atmospheric
Chemistry
and Physics
Discussions

259   Level 2 products are provided as granules with a spatial resolution of 10 km at nadir.

260   The standard deviation on the AOD retrieval (Remer et al., 2005) over land (ocean) is

261   0.15±0.05xAOD (0.05±0.03xAOD). We also use level 3 daily sea surface temperature

262   (SST) data derived from the 11 μm thermal infrared band available at 9.26 km spatial

263   resolution for daytime passes (Werdell et al., 2013).

264

265   The hourly land surface temperature products from the Copernicus Global Land

266   Service (https://land.copernicus.eu/global/products/lst) used in this study are

267   available at 5 km spatial resolution. The radiative skin temperature of the land

268   surface is estimated from the infrared spectral channels of sensors onboard a

269   constellation of geostationary satellites (among which SEVIRI on MSG). Its estimation

270   further depends on the surface albedo, the vegetation cover and the soil moisture.

271

272   The Cloud-Aerosol LIdar with Orthogonal Polarization (CALIOP) flies onboard the

273   Cloud-Aerosol Lidar Pathfinder Satellite Observation (CALIPSO), following a similar

274   polar orbit than Aqua within the A-train constellation. In this work, we use CALIOP

275   level-2 data (version 4.10) below 8 km above mean sea level (amsl; https://www-

276   calipso.larc.nasa.gov/products/). Details on the CALIOP instrument, data acquisition

277   and science products are given by Winker et al. (2007). We mainly consider the

278   aerosol typing, which was corrected in version 4.10, as described in Burton et al.

279   (2015).

280

281   2.3 Radiosounding network

282

283   During the DACCIWA field campaign, the upper air network was successfully

284   augmented in June and July 2016 to a spatial density unprecedented for SWA (see

285 Flamant et al., 2018). In this study, we use radiosounding data from meteorological

286 balloons launched in Abidjan, Accra and Cotonou in the afternoon of 2 July (see

287 **Figure 1**). The management of soundings at Abidjan and Cotonou was

288 subcontracted to a private company, while the Ghana Meteorological Agency took

289 care of the soundings in Accra. The Karlsruhe Institute of Technology was instrumental

290 in the Ghana sounding and staff from the Agence pour la Sécurité de la Navigation

291 Aérienne en Afrique et à Madagascar helped with the Abidjan and Cotonou

292 soundings.

293

294   3. Models and simulations

295

296   3.1 ECMWF operational analyses & CAMS forecasts

297

298 For the investigation of atmospheric dynamics at the regional scale, we use

299 operational analyses from the Integrated Forecasting System (IFS, a global data

300 assimilation and forecasting system) developed by the European Centre for Medium-

301 Range Weather Forecasts (ECMWF). The analyses presented in this paper are

302 associated with IFS model cycle CY41r2. The original $T_{CO}1279$ (O1280) resolution of the

303 operational analysis was transformed onto a 0.125° regular latitude-longitude grid.

304 Long-range transport of biomass burning and dust laden air masses transported over

305 the Gulf of Guinea are monitored with respective optical depths at 550 nm

306 calculated from the ECMWF Copernicus Atmosphere Monitoring Service-Integrated

307 Forecasting System (CAMS-IFS; Flemming et al., 2015) available at a resolution of 0.4°.

308

309   3.2 WRF and CHIMERE simulations

310

311   The WRF model (version v3.7.1, Shamarock and Klemp, 2008) and the CHIMERE

312   chemistry-transport model (2017 version, Mailler et al., 2017) are used in this study.

313   WRF calculates meteorological fields that are then used by CHIMERE to (i) conduct

314   tracer experiments and (ii) compute backplumes. WRF and CHIMERE simulations are

315   performed on common domains. For the period 30 June—3 July 2016, two simulations

316   are conducted to provide insights into the airborne observations: a simulation with a

317   10-km mesh size in a domain extending from 1°S to 14°N and from 11°W to 11°E

318   (larger than the domain shown in **Figure 1a**) and a simulation with a 2-km mesh size in

319   a domain extending from 2.8°N to 9.3°N and from 2.8°W to 3.3°E (**Figure 1a**). The 10-

320   km WRF simulation uses National Center for Environmental Prediction (NCEP) Final

321   global analyses as initial and boundary conditions. NCEP Real-Time Global SSTs

322   (Thiébaux et al., 2003) are used as lower boundary conditions over the ocean. The

323   meteorological initial and boundary conditions for the 2-km WRF simulation are

324   provided by the 10-km WRF run. The simulations are carried out using 32 vertical

325   sigma-pressure levels from the surface to 50 hPa, with 6 to 8 levels in the ABL for WRF

326   and with 20 levels from the surface to 300hPa for CHIMERE. This model configuration is

327   the same as described in Deroubaix et al. (2018).

328

329   The representation of the atmospheric dynamics in the 2-km simulation was verified

330   against dynamical and thermodynamical observations from both aircraft (**Figure S1**)

331   and the DACCIWA radiosounding network from Accra and Cotonou (**Figure S2**),

332   yielding satisfactory results.

333

334   3.2.1   Tracer experiments

335

336   A series of numerical tracer experiments were conducted to aid interpreting airborne

337   observations, particularly by separating (locally emitted) urban pollution from long-

338   range transported aerosol plumes. Passive tracers were set to be released from four

339   major coastal cities: Accra (Ghana, 5.60°N, 0.19°W), Lomé (Togo, 6.17°N, 1.23°E),

340   Cotonou (Benin, 6.36°N, 2.38°E) and Lagos (Nigeria, 6.49°N, 3.36°E). We conducted

341   two sets of experiments: one for which emissions from the cities are identical (TRA_I,

342   with "I" standing for "identical") and one for which the emissions are different and

343   proportional to the size of the population (TRA_D, with "D" standing for "different"),

344   based on the World Urbanization Prospect report (2015). In the latter case, emissions

345   from Lomé, Accra and Lagos are scaled to Cotonou emissions (1.8, 3 and 13 times,

346   respectively). Tracers are emitted in the lowest level of the model (below 10 m

347   altitude) during the period of interest: in experiences TRA_D1 and TRA_I1, tracers are

348   emitted continuously on 1 and 2 July, while in experiences TRA_D2 and TRA_D3,

349   tracer emissions only occur on 1 July and 2 July, respectively. Emissions take place in

350   a 2 km x 2 km mesh for each city. For the sake of simplicity, emissions are constant in

351   time and thus do not have a diurnal cycle. Tracer concentrations in the atmosphere

352   are then shown in arbitrary units (a.u.) and colored according to the city: blue for

353   Accra, green for Lomé and red for Cotonou. By design, the lifetime of the tracers

354   emitted at a given time from any of the considered cities is 48h. After that time,

355   tracers have either moved out of the domain or their concentration is set to zero.

356

357   3.2.2   Backplumes

358

359   Backplumes (or back trajectory ensembles) are computed according to Mailler et al.

360   (2016), using a dedicated regional CHIMERE simulation with a mesh size of 30 km,

361   covering the whole of Africa. For this study, 50 tracers are released at the same time

Atmospheric
Chemistry
and Physics
Discussions

362   for selected locations along the ATR 42 flight trajectory, where large aerosol contents

363   are observed: (i) the southernmost part of the flight (2.0°W, 4.5°N) and (ii) the

364   northernmost part of the flight (1.0°E, 5.5°N). For both locations, backplumes are

365   launched at 2500 m above sea level on 2 July 2016 at 17:00 UTC. Very similar results

366   are obtained for both backplumes. Hence, in the following we shall only show results

367   from the backplume released from the northernmost location.

368

369   4.   Synoptic situation and airborne operations on 2 July 2016

370

371   The entire DACCIWA aircraft campaign took place during WAM post-onset

372   conditions (Knippertz et al., 2017), i.e. after the migration of the climatological

373   precipitation maximum from the coast to the Sahel, with the monsoon flow being

374   well established over SWA. The campaign also took place after the onset of the

375   Atlantic Cold Tongue as evident in Figure 3 of Knippertz et al. (2017), which also

376   highlights that the coastal upwelling started progressively building up around 27 June

377   2016.

378

379   In the period spanning from 29 June to 5 July 2016, the major weather disturbances

380   over SWA are associated with African Easterly Waves traveling along a well-

381   organized African Easterly Jet (AEJ). A cyclonic center propagating to the south of

382   the AEJ (identified from ECMWF 850 hPa streamline charts, not shown) originated

383   from eastern Nigeria on 29 June, sweeping through SWA during the following days.

384

385   On 2 July 2016, the cyclonic center is located at the coast of Sierra Leone (see

386   disturbance labelled "F" in Fig. 14 of Knippertz et al., 2017). The monsoonal winds are

387   almost southerly over the Gulf of Guinea (south of 4°N) and progressively veer to

388 southwesterly farther north and over the continent (**Figure S3a**). In the mid-

389 troposphere, SWA is under the influence of easterly flow conditions (**Figure S3b**). West

390 of 5°E, the AEJ is located over the Sahel and is intensified along its northern boundary

391 by a strong Saharan high located over Libya. The AEJ maximum is seen off the coast

392 of Senegal.

393

394 The region of interest experiences high insolation on 1 July with temperatures in the

395 30s °C across SWA and widespread low-level clouds dissolving rapidly in the course of

396 the morning. On 2 July, there is a clear indication of land-sea breeze clouds in the

397 high-resolution SEVIRI image at 1200 UTC (**Figure 2a**) with relatively cloud-free

398 conditions over the ocean, where the ATR 42 flew later on. The land-sea breeze front

399 is seen in-land to follow the coastline from western Ghana to western Nigeria. The

400 front is observed to move farther in-land until 1500 UTC (**Figure 2b**) with shallow

401 convective cells forming along it. Farther south the area is free of low-level clouds

402 (both over land and ocean). Oceanic convection occurred offshore on the previous

403 day and mesoscale convective systems were present over north-central Nigeria in

404 the morning of 2 July. Satellite images show both oceanic and inland convection to

405 be decaying by midday (**Figure 2a**).

406

407 On 2 July, the ATR 42 aircraft took off from Lomé at 1445 UTC (*NB: UTC equals local*

408 *time in July in Togo*) and headed towards the ocean, flying almost parallel to the

409 Ghana coastline (**Figure 1a**) at low level (in the marine ABL). Before reaching the

410 Cape Three Points (close to the border between Ghana and Ivory Coast), the ATR 42

411 changed direction and headed south. Upon reaching its southernmost position

412 (~3°N), the ATR 42 turned around and climbed to 3200 m amsl and finally headed

413 back to Lomé at that level. On the way back, the aircraft changed heading around

Atmospheric
Chemistry
and Physics
Discussions

414   1653 UTC to fly along the coast prior to landing. The ATR 42 passed the longitude of

415   Accra at 1729 UTC and landed in Lomé at 1807 UTC. The high-level flight back

416   allowed mapping out the vertical distribution of aerosols and clouds using the lidar

417   ULICE. In situ aerosol and gas phase chemistry measurements will be used in the

418   following to characterize the composition of aerosols and related air masses

419   sampled with the lidar, particularly during the ascent over the ocean (between 1633

420   and 1647 UTC), the elevated leveled run and the descent towards the Lomé airport

421   (between 1753 and 1807 UTC).

422

423   5. Atmospheric composition over the Gulf of Guinea and the link with lower

424   tropospheric circulation

425

426   **Figure 3** shows ULICE-derived ASR and VDR cross-sections acquired between 1640

427   UTC and 1800 UTC, including data gathered during the aircraft ascent over the

428   ocean and descent in the vicinity of the coast. It is worth noting that most of the lidar

429   data shown in **Figure 3** were acquired while the aircraft was flying along the

430   coastline (from 1653 UTC on). Wind measurements from the Abidjan, Accra and

431   Cotonou soundings as well as from the ATR 42 sounding over the ocean clearly show

432   that above 1.2 km amsl the flow is easterly over the region of aircraft operation

433   (**Figure 4**). Given that the heading of the aircraft along this elevated leg is 65°, the

434   lidar "curtains" above 1.2 km amsl in **Figure 3** are mapping out aerosol layers that are

435   transported westward (with the ATR 42 flying against the mean flow).

436

437   Several outstanding features are highlighted in **Figure 3**. Generally few clouds were

438   encountered along the flight track (they appear in dark red colors). Exceptions are

439   the low-level clouds at the top of the marine ABL with a base around 500 m amsl to

17

Atmospheric
Chemistry
and Physics
Discussions

440   the west of the track between 1655 and 1702 UTC (**Figure 3a**). The vertical extension

441   and the number of the cumulus clouds topping the marine ABL decreases towards

442   the east. This shoaling of the marine ABL is likely ascribed to the increasing trajectory

443   length of near-surface parcels over the cold coastal waters (as the aircraft flies over

444   the coastal upwelling region). Near Lomé, the top of the marine ABL can only be

445   identified from the higher ASR values reflecting the impact of high relative humidity

446   on the scattering properties of the marine aerosols (**Figure 3a**). An isolated deeper

447   convective cloud is observed before 1648 UTC between 2 and 2.5 km, which is also

448   sampled in situ by the ATR 42 cloud probes. The top of the cloud is likely connected

449   to a temperature inversion observed during the aircraft ascent over the ocean (not

450   shown). High lidar-derived ASRs are observed near the marine ABL top and to some

451   extent in the mixed layer (**Figure 3a**). The ASR-enhanced layers do not show on the

452   VDR plot, Possibly because they are related to the presence sea-salt aerosols which

453   are spherical particles that do not depolarize the backscattered lidar signal.

454   However, the high ASR values could also be related to the advection of biomass

455   burning aerosols from the south in the marine ABL (e.g. Menut et al., 2018) as

456   suggested by the relatively high CO and extinction coefficient values observed in

457   the ABL over the ocean (110 ppb and 50 Mm^{-1}, respectively) in Figure 4c and 4e.

458   Biomass burning aerosols are also generally associated with low VDR values.

459

460   In addition to clouds and marine ABL aerosols, several distinct aerosol features in the

461   free troposphere stand out from the lidar plot:

462   • **Features A and B** correspond to plumes with high values of ASR (larger than 1.2)

463   and VDR (larger than 0.8%) observed near the coast between the surface and 0.5

464   km amsl and between 0.5 and 1.5 km amsl, respectively, during the aircraft

465   descent towards Lomé. According to the aircraft in situ observations, feature B is

466 located in a strong wind shear environment at the top (~600 m) of the ABL (**Figure**

467 **4**) with its upper part being located in the easterly flow, while feature A is

468 associated with a south-southwesterly flow. This sheared environment likely

469 explains the slanted structure of the aerosol plume associated with feature B.

470 • **Feature C** is an intermediate aerosol layer characterized by VDR values lower than

471 those for feature B, suggesting more spherical (possibly more aged pollution)

472 aerosols. This feature is bounded by much lower VDR values, especially above,

473 while being associated with higher ASR values than its immediate environment.

474 This feature is slanted between Lomé and the deeper isolated cloud. The layer

475 thickness is larger near Lomé than over the more remote ocean, leading to a less

476 slanted layer top. This layer has also been sampled in situ by the ATR 42 during its

477 ascent over the ocean. It is characterized by VDRs on the order of 0.7%. Based on

478 the aircraft sounding data, it appears that this layer is mostly advected with the

479 easterly flow above 1.2 km amsl (**Figure 4**).

480 • **Feature D** is an elevated aerosol layer observed at the level of the aircraft (i.e. at

481 3200 m amsl) in the vicinity of Lomé, which was also sampled in situ by the ATR 42.

482 This layer is separated from feature B by a ~500 m deep layer of non-depolarizing

483 aerosols (very low VDRs). The base of this layer exhibits a slanting similar to the one

484 observed for the top of the intermediate aerosol layer (feature B). Large VDRs are

485 found in the core of this feature (> 1.2%). It appears that this layer is also advected

486 with the easterly flow above 1.2 km amsl.

487 • **Feature E** is also an elevated aerosol layer, but observed farther south over the

488 ocean and in the vicinity of the isolated deeper cloud. It is characterized by large

489 ASR values but low VDR values (suggesting the presence of low-depolarizing

490 aerosols).

491

Atmospheric
Chemistry
and Physics
Discussions

492   Given the distance of the oceanic profile to the coast (~100 km), we consider the

493   oceanic (ascending) profile as representative of background aerosol/gas phase

494   conditions upstream of coastal SWA. Using this profile as reference, we have

495   analyzed the characteristics of the aerosol plume sampled with the ATR 42 (both in

496   situ and remotely) during the aircraft descent over Lomé. The most significant

497   differences between the ATR 42 observations acquired during the oceanic profile

498   and the profile over Lomé are found below 1.7 km amsl (**Figure 5**) and are

499   associated with features A and B.

500

501   ATR 42 observations associated with feature A (below 0.5 km amsl) show increases in

502   NO_x, CO and PM1 aerosol concentrations (**Figure 5a, c, f**, respectively) as well as

503   extinction coefficient (**Figure 5e**), together with an O_3 concentration reduction

504   (**Figure 5b**). No CPC-derived aerosol concentrations are available below 0.5 km

505   amsl. The few PSAP measurements made around 0.5 km amsl during the descent

506   yield an AAE value around ~1 (**Figure 5g**). Furthermore, the ratio of O_3 to CO

507   concentrations is on the order of 0.15 (not shown). These are solid indications that the

508   ATR 42 sampled a fresh urban anthropogenic plume near Lomé (Brito et al., 2018),

509   advected with the south-southwesterly monsoon flow (the ATR 42 being downstream

510   of Lomé then).

511

512   ATR 42 observations associated with feature B (between 0.5 and 1.5 km amsl) show

513   increases in concentrations for all variables under scrutiny, including O_3. The latter

514   (**Figure 5b**) is the most significant difference between the characteristics of features B

515   and A. Other differences include the much smaller increases in CO concentration

516   and OPC aerosol (N_{PM1}, $N_{PM2.5}$ and N_{PM10}) concentrations as well as extinction

517   coefficients observed in feature B (**Figure 5c, e, f**, respectively). The O_3/CO ratio is

Atmospheric
Chemistry
and Physics
Discussions
Open Access
EGU

518 also larger (i.e. 0.25, not shown) than that associate with feature A. These

519 observations, together with wind measurements, suggest that feature B corresponds

520 to a more aged urban plume. This could be an indication that the ATR 42 sampled

521 more than just the Lomé plume. This will be investigated using tracer experiments in

522 Section 6. Above 2 km amsl, the AAE increases to larger values (> 1.5), evidencing a

523 change in aerosol nature, i.e. a transition from local urban emissions to elevated

524 background pollution (**Figure 5g**), possibly resulting from a mixture long-lived

525 anthropogenic pollution and long-range transport of dust and biomass burning

526 aerosols from previous days.

527

528 Regarding feature C, the in situ measurements do not allow characterizing the

529 nature of the aerosols. The origin of this layer will also be investigated using tracer

530 experiments (see Section 6).

531

532 The in situ measurements along the elevated ATR 42 track reveal significant

533 differences in aerosol/gas phase concentrations and properties between the

534 western part (where feature E is observed with the lidar) and the eastern part (where

535 feature D is observed) of the ATR 42 leg (**Figure 6**). In the western part, ATR 42

536 measurements highlight enhanced O_3 and CO concentrations (> 60 ppbv and

537 > 200 ppvb, respectively, **Figure 6a, b**) together with AAE values of ~1.5 (**Figure 5f**),

538 suggesting the presence of biomass burning aerosol. Furthermore, aerosol number

539 concentrations N_{PM1} and N_{10} show enhanced values for small particles (100 # cm^{-3}

540 and ~1000 # cm^{-3}, respectively, **Figure 6c, d**). The observed O_3, CO and N_{10}

541 concentrations are larger than the background values measured during the ascent

542 over the ocean (~40 ppbv, 150 ppbv, and 500 # cm^{-3}, respectively, **Figure 5b, c, f**).

543 Large extinction values are also observed (100 Mm^{-1}), largely exceeding the

544 background value of 30 Mm^{-1}(compare **Figure 6e and Figure 5e).**

545

546 In the eastern part of the leg, AAE values of ~1.5 also suggest that biomass burning

547 aerosols are sampled. O3, CO, N_{PM1} and N_{10} concentrations diminish approximately

548 half way through the leg to their background values (from 1716 UTC on, **Figure 6a, b,**

549 **c, d**), as does the extinction coefficient. However, $N_{PM2.5}$ and N_{PM10} concentrations

550 increase significantly, as opposed to N_{PM1}, which combined with enhanced lidar-

551 derived VDR suggest mixing with larger particles, possibly dust. Further insight into the

552 origin of these aerosols, observed as a result of long-range transport, will be

553 investigated in Section 7.

554

555 Finally, in Section 8 we will investigate the cause of the slanting of the elevated

556 aerosol layers from west to east along the flight track, which also possibly leads, in

557 addition to the colder SSTs, to a thinning of the marine ABL and the suppression of

558 clouds at its top in the vicinity of Lomé (**Figure 3**).

559

560   6. Tracer experiments for anthropogenic aerosols

561

562 The objectives of the tracer experiments are threefold: (i) understand how the lower

563 tropospheric circulation shapes the structure of the urban pollution plume emitted

564 from coastal cities and observed with the ULICE lidar (marked A and B in **Figure 3**), (ii)

565 assess which cities contribute to the plume observed with ULICE and whether it results

566 from Lomé emissions only, and (iii) provide insight into the origin of the intermediate

567 aerosol layer (marked B in **Figure 3**). For this we have analyzed along the ATR 42

568 aircraft flight track the tracer simulations introduced in Section 3.

569

570   As an ancillary objective, we also aim to assess how far over the ocean the urban

571   pollution aerosols can be transported by the complex low-level circulation over SWA.

572   For this, we have analyzed the tracer simulations along four 0.5°-wide north–south

573   transects spanning the longitudinal range of the ATR 42 flight (centered at 0.75°W,

574   0.25°W, 0.25°E and 0.75°E, cf. **Figure 1b**).

575

576   6.1 Structure of the urban plume along the coastline

577

578   **Figure 7** shows the structure of the urban pollution plume along the aircraft track

579   between 1400 and 1800 UTC in the TRA_D and TRA_I experiments. In TRA_D1 (**Figure

580   7a**), feature A as observed in the lidar VDR field (**Figure 3**) corresponds to emissions

581   from Lomé only (in greenish colors) in the ABL (blue dotted line), while feature B

582   corresponds to emissions from Lomé mainly with a contribution from Accra

583   (superimposed with the Lomé plume) and Cotonou (reddish colors in the upper

584   western boundary of the Lomé plume). In the TRA_I1 experiment, the Accra

585   contribution is missing altogether (**Figure 7b**). More strikingly, TRA_D1 shows an

586   elevated tracer plume over the ocean originating from Accra (blueish colors), which

587   mimics feature C in **Figure 3** fairly well. This feature is almost absent in TRA_I1, stressing

588   the importance of accounting for enhanced emissions from Accra (with respect to

589   Lomé and Cotonou) to produce a more realistic tracer simulation.

590

591   Results from experiment TRA_D2 (**Figure 7c**) shows that feature C in the lidar VDR

592   observations is likely related to emissions from Accra from the previous day only (i.e. 1

593   July), as the structure of the Accra plume in TRA_D1 and TRA_D2 is the same. In this

594   experiment, the structures of the plume corresponding to features A and B in **Figure 3**

Atmospheric
Chemistry
and Physics
Discussions

595   are clearly altered by the lack of recent emissions in Lomé on 2 July (the lower part of

596   the plume is likely advected northward with the southerly flow here). This is confirmed

597   by looking at the result of TRA_D3 (**Figure 7d**): the fresh emissions (on 2 July) from

598   Lomé do lead to a realistic simulation of the shape of features A and B observed by

599   lidar. On the other hand, feature C is not reproduced in this experiment, suggesting

600   that feature B as observed by lidar is a mix of fresh and more aged emissions from

601   Lomé, as well as aged emissions from Cotonou and Accra, while feature C is almost

602   entirely related to aged pollution from Accra. What is also worth noting is that no

603   emissions from Lagos on 1 and 2 July are observed along the ATR 42 flight track in the

604   TRA_D and TRA_I experiments.

605

606   6.2 Southward transport of the urban plume over the Gulf of Guinea

607

608   **Figure 8** shows the structure of the urban pollution plume along four 0.5°-wide north–

609   south transects centered at 0.75°W, 0.25°W, 0.25°E and 0.75°E on 2 July at 1600 UTC,

610   i.e. half way through the ATR 42 flight.

611

612   Along the westernmost transect, labeled I in **Figure 1b** (centered at 0.75°W), the

613   pollution plume is only composed of emissions from Accra and is lifted off the surface

614   above the ABL (**Figure 8a**). Note that no tracer emissions directly occur in this

615   transect, with Accra emissions being contained in transect II, to the east of transect I.

616   As discussed by Knippertz et al. (2017), during the campaign, pollution plumes from

617   coastal cities were mostly directed northeastwards (see their Figure 19). Hence the

618   tracer plume seen in the experiment on 2 July is associated with transport of tracers

619   emitted on 1 July in the monsoon flow toward the northeast, which are then vertically

620   mixed (due to thermally and mechanically driven turbulence), and westward

Atmospheric
Chemistry
and Physics
Discussions
Open Access
EGU

621 advection of the tracers by the easterly flow above the monsoon layer. Over the

622 ocean, the plume is seen to extend as far south as 4.7°N, i.e. the southernmost

623 extension seen on all transects shown in **Figure 8**. This is linked to a small equatorward

624 component in the easterly flow (not a meridional overturning circulation).

625

626 Along the transect centered at 0.25°W (transect II, **Figure 1b**), the plume is seen to be

627 in contact with the surface as far north as 6.5°N (**Figure 8b**). The strong ascent at 6°N

628 is related to the presence of the Mampong range in the Ashanti uplands (see **Figure**

629 **1b**). The presence of the range and the associated motion contributes to deep

630 mixing of the plume north of Accra with the top of the tracer plume reaching 4 km

631 above the ground level or higher. Strong subsidence is seen north of the Mampong

632 range that mixes tracers down to the surface. Other ascending and subsiding

633 motions are detectable over the Lake Volta area, which could be related to land-

634 lake breeze systems. South of 6°N, the tracer plume is as deep as along transect I,

635 but does not extend southward over the ocean. Here also, only emissions from Lomé

636 contribute to the pollution plume on 2 July, suggesting that it took 24 h for these

637 emissions to reach transect II.

638

639 The pollution plume along the transect centered at 0.25°E (transect III) is structurally

640 similar to the one along transect II, but reaches farther inland (~7.5°N at the surface,

641 **Figure 8c**) than in transect II, likely due to the gap between the Mampong range

642 and the Akwapim-Togo range, and the flat terrain around Lake Volta. Again,

643 ascending and subsiding motions are detectable over the Lake Volta area that

644 could be related to land-lake breeze systems. Over the ocean, the plume reaches

645 5.3°N at 1.5 km amsl. Emissions from Lomé and Cotonou contribute to the upper and

646 southernmost part of the tracer plume along this transect, just north of 5.6°N.

Atmospheric
Chemistry
and Physics
Discussions

647

648   Finally, along transect IV, the composition of the urban pollution plume is dominated

649   by emissions from Accra, with a small contribution of emissions from Cotonou and

650   Lomé in the southern, uppermost part of the plume because of short-range

651   westward transport above the monsoon flow (**Figure 8d**). The Accra plume is seen to

652   extend from the coastline to as far as 9°N and above the depth of the continental

653   ABL, but not as deep as along other transects with more pronounced orography. The

654   northward extension of the plume suggests that emissions from Accra are

655   transported over Togo along the eastern flank of the Akwapim-Togo range. Over the

656   ocean, the upper part of the plume barely reaches 5.6°N at an altitude of 2 km amsl.

657

658   The differences seen in the structure of the pollution plume obtained from the tracer

659   experiment over land are likely due to interactions between the monsoon flow and

660   the orography just to the north of Accra: namely the southeast–northwest running

661   Mampong range and the north-south running Akwapim-Togo range to the east of

662   Accra, both bordering Lake Volta (**Figure 1b**). In addition to those orographic effects,

663   the monsoon flow transporting the tracers towards the north may also interact with

664   the land-lake breeze system occurring in the summer over Lake Volta (Buchholz et

665   al., 2017a, b). Addressing the impact of these complex circulations over land on the

666   urban pollution plumes is beyond the scope of this paper.

667

668   Strikingly, as in the along aircraft flight track cross-section, emissions from Lagos on 1

669   and 2 July are never seen in the north-south transects, confirming that they likely do

670   not impact on the air quality in the major coastal cities to the west during this period.

671   Furthermore, the tracer simulations suggest that the pollution plume over SWA

672   related to emissions in the four cities considered here does not extend very far over

Atmospheric
Chemistry
and Physics
Discussions

673   the ocean (to 4.7°N at most), essentially because they are transported northward

674   within and westward above the marine ABL. Nevertheless, the western part of the

675   Accra pollution plume spreads farther south over the ocean than the eastern part.

676

677   7. Long-range transport of aerosols related to regional-scale dynamics

678

679   To gain insights into the origin of the aerosol layers sampled by the ATR along the

680   elevated leg and observed by lidar (features D and E in **Figure 3**), 10-day back-

681   trajectories ending at 2500 m amsl at 1700 UTC on 2 July are computed using

682   CHIMERE. The backplume associated with feature D is shown in **Figure 9a** (the one

683   associated with feature E is nearly identical and will not be discussed). The back

684   trajectories suggest that feature D originates from a broad area including Gabon,

685   Congo and the Democratic Republic of Congo. Most of the back trajectories then

686   travel over the Gulf of Guinea towards SWA in the free troposphere (**Figure 9b**). Daily

687   mean AOD derived from MODIS and SEVERI observations on 2 July (**Figure 10a**) show

688   large values offshore of Gabon and Congo known to be biomass burning aerosol

689   emission hotspots at this time of year (e.g. Menut et al., 2018). This is corroborated by

690   the CAMS biomass burning aerosol forecast at 1200 UTC (**Figure S4a**).

691

692   The afternoon CALIOP observations acquired to the east of the ATR 42 flight track

693   across the enhanced AOD feature (see track in **Figure 10a**) indeed classify the

694   aerosols over the ocean as elevated smoke, transported between 1.5 and 4 km amsl

695   (**Figure 10b**). The altitude of transport is consistent with that derived from the CHIMERE

696   backplume (**Figure 9b**) as also shown by Menut et al. (2018). Along this transect, dust

697   is observed to almost reach the SWA coastline from the north (**Figure 10b**) consistent

698   with the moderate AOD values observed over Togo and Benin (**Figure 10a**).

Atmospheric
Chemistry
and Physics
Discussions

Open Access

EGU

699   Furthermore, the morning ATR 42 flight conducted on 2 July in the region of Savè

700   (Benin, ~8°N) highlighted the presence of dust over northern Benin (Flamant et al.,

701   2018). Interestingly, at the coast (~6°N), CALIOP shows evidence of polluted dust,

702   possibly resulting from the mixing of dust with anthropogenic emissions from coastal

703   cities. However, the CAMS forecast does not show dust reaching the SWA coast

704   (**Figure S4b**).

705

706   The backplume and regional scale dynamics analyses indicate that the upper-level

707   aerosol features D and E (as observed by lidar) are related to biomass burning over

708   Central Africa. In the case of feature D, closer to Lomé, MODIS, SEVIRI and CALIOP

709   observations suggest the possibility of mixing with dust, consistently with the ATR in situ

710   and lidar-related observations.

711

712   8.   Coastal circulations: the role of surface temperature gradients and orography

713

714   IFS vertical velocity computed between 850 and 600 hPa (i.e. above the monsoon

715   flow) shows that most of the northern Gulf of Guinea is under the influence of

716   subsiding motion on 2 July at 1800 UTC (**Figure 11b**). Stronger subsidence is seen to

717   the east of the region of operation of the ATR 42 at that time. Strong subsidence is

718   also seen over the eastern part of the ATR 42 flight track at 1200 UTC (**Figure 11a**).

719   However, at 1200 UTC, the eastern part of the northern Gulf of Guinea is

720   characterized by upward motion, possibly in relationship with the SST gradient (cold

721   water to the west linked with the coastal upwelling and warmer waters to the east in

722   the Niger delta region). The signature of the sea breeze is also visible inland in the IFS

723   analysis at 1200 UTC (**Figure 11a**) in the form of a line of strong ascendance running

724   parallel to the coastline.

Atmospheric
Chemistry
and Physics
Discussions

725

726   At the regional scale, IFS analyses evidence the existence of marked surface

727   temperature difference between the ocean and the continent at 1200 UTC (**Figure**

728   **S5d**) because of the high insolation across SWA as noted in Section 2. The surface

729   temperature gradient across the coast creates shallow overturning circulations as

730   evidenced by IFS analyses at 1800 UTC (**Figure 12**). A well-defined closed zonal cell

731   can be identified below 600 hPa around 5°N and between 0°E and 8°E (**Figure 12a**),

732   while a well-defined meridional cell is seen around 0°E between 3°N and 8°N (**Figure**

733   **12c**). It is worth noting that the overturning circulations are most intense and better

734   defined at 1800 UTC than at 1200 UTC (compare **Figure 12a** with **Figure S5c** for the

735   zonal cell), even though the surface temperature difference across the coast is

736   weaker (compare **Figure 12b** with **Figure S5d**). The overturning circulation exhibits a

737   strong diurnal cycle (**Figure S5**), which is driven by the surface temperatures over

738   land. The quality of IFS skin temperature during the day was verified against observed

739   land surface temperature observations (so-called Copernicus product; see **Figure**

740   **S6**). In spite of a systematic bias on the order of 2°C over land, IFS skin temperature

741   analyses are seen to be consistent (in terms of spatio-temporal distribution) with the

742   Copernicus product (**Figure S6**). This gives us confidence that the overturning

743   circulations exists and contributes to enhance subsidence over the Gulf of Guinea.

744   Furthermore, we have conducted an analysis of the correlation between the land-

745   sea skin temperature gradients associated with both the zonal and the meridian cells

746   and the vertical velocity over the Gulf of Guinea at different times of day for the

747   whole of July 2016, based on IFS data (**Table 2**). The analysis shows that the zonal

748   land-sea skin temperature gradient at 1200 and 1800 UTC is significantly correlated

749   with vertical velocity at 1800 UTC with values around 0.5. On the other hand, the

750   meridional land-sea skin temperature gradient at 1200 UTC is correlated (0.34) with

751 vertical velocity at 1200 UTC, possibly due to the presence of orography as discussed

752 in the following. Hence, the overturning cells evidenced on 2 July appear to be

753 persistent features over the Gulf of Guinea, at least in post-monsoon onset

754 conditions.

755

756 In addition to the subsidence generated at the regional scale by the land-sea

757 temperature gradient, the interaction of the monsoon flow with the orography over

758 Ghana and Togo is responsible for more local coastal circulations. This interaction is

759 reflected in the vertical velocity anomaly simulated with WRF along the western- and

760 easternmost transects in **Figure 1b** (transects I and IV, respectively). The anomalies

761 are computed with respect to the average vertical velocity between 1°W and 1°E.

762 **Figure 13** shows that in the region where orography is more pronounced (i.e. to the

763 west), the vertical velocity anomaly is positive, while it is negative to the east where

764 orography is less marked (compare **Figure 13a** and **13b**). As a result, the eastern

765 region of ATR 42 operation on 2 July is under the influence of strong subsiding motion.

766 This subsiding motion suppresses low-level cloudiness near Lomé and is key to the

767 interpretation of the ATR 42 lidar observations along the track regarding the slanting

768 of the elevated aerosol layers and, possibly, the thinning of the marine ABL towards

769 the eastern end of the aircraft track, together with an additional effect of colder

770 SSTs.

771

772 MODIS observations show the existence of an SST dipole across the northern part of

773 the Gulf of Guinea (**Figure S7** and **Figure 11**), between the coastal upwelling offshore

774 of Lomé and Accra (SSTs on the order of 26°C) and the warmer SST to the east in the

775 Bight of Bonny (offshore Nigeria, where SST on the order of 28°C are generally

776 observed). Even though this SST dipole may also generate a secondary circulation

777   over the Gulf of Guinea (e.g. around 900-800 hPa and between 0 and 1°E in **Figure**

778   **S5c**), it is very likely that the lower tropospheric dynamics in the region of operation of

779   the aircraft are dominated by the monsoon dynamics to the first order and by the

780   sea-land surface temperature gradient at the regional scale.

781

782   9. Summary and conclusions

783

784   In this study, detailed aircraft observations and accompanying model simulations

785   were used to analyze the distribution of aerosols over the Gulf of Guinea and its

786   meteorological causes. We show that land-sea surface temperature gradients

787   between the northern part of the Gulf of Guinea and the continent as well as

788   orography over Ghana and Togo play important roles for the distribution of aerosols

789   and gases over coastal SWA. The former creates large-scale subsidence conditions

790   over the northern part of the Gulf of Guinea through the generation of zonal and

791   meridional overturning circulations below 600 hPa, with the downward branch of the

792   circulation around 0°E over the ocean. The latter generates enhanced subsidence

793   over the eastern part of the ATR 42 operation area, near Lomé and Accra. Together

794   this leads to a west–east tilting of the aerosol layers (that can be considered as

795   passive tracers of the dynamics) along the flight track. The ATR 42 sampled remotely

796   and in situ the complex aerosol layering occurring between 2.5 and 3.2 km amsl over

797   the Gulf of Guinea as a result of long-range transport of dust (from the northeast)

798   and biomass burning aerosol from the south (feature E in **Figure 3**) and the mixing

799   between these (feature D).

800

801   The orography-forced circulation also has an influence on the structure of the urban

802   pollution plumes from Accra, Lomé and Cotonou as assessed from airborne lidar

Atmospheric
Chemistry
and Physics
Discussions

803   measurements and numerical passive tracer experiments using the WRF model.

804   When accounting for the relative size of the emitting cities along the coast (3 times

805   more emissions in Accra than in Lomé), we find that the tracer experiment designed

806   to include emissions from 1 and 2 July is the most realistic in reproducing the lidar

807   observations. The analysis shows that (a) the large pollution plumes observed at the

808   coast up to 1.5 km (features A and B) are essentially related to emissions in the Lomé

809   area from both 1 and 2 July, with a moderate contribution from Accra and Cotonou,

810   (b) the elevated plume over the northern part of the Gulf of Guinea (feature C) is

811   related to emissions from Accra exclusively from the day before the ATR 42 flight (i.e.

812   1 July) and these clearly dominate the composition of the tracer plume in the region

813   covered by the flight track on 2 July, (c) Lagos emissions (taken to be 20 times that of

814   Lomé) do not appear to be a player for regions west of Lomé in the summer in post-

815   onset conditions as also shown by Deroubaix et al. (2018), and (d) the tracer plumes

816   do not extend very far over the ocean, mostly because they are transported

817   northward within and westward above the marine ABL.

818

819   The unique combination of in situ and remote sensing observations acquired over

820   the Gulf of Guinea during the 2 July OLACTA flight together with global and regional

821   model simulations revealed in details the impact of the complex atmospheric

822   circulation at the coast on the aerosol composition and distribution over the northern

823   Gulf of Guinea. We show that the western Gulf of Benin is a place favorable for

824   subsidence in the afternoon due to 3 factors, namely cool SSTs, zonal overturning

825   connected with the Niger Delta region and meridional overturning connected with

826   the main West African landmass, anchored geographically at the Mampong and

827   Akwapim-Togo ranges. We also show that the overturning cells are robust features of

828   the atmospheric circulation over the Gulf of Guinea in July 2016. To the best of the

Atmospheric
Chemistry
and Physics
Discussions

829   authors' knowledge such features have not been documented in the literature to

830   date.

831

832   Further research will be dedicated to enhance our understanding of the complex

833   interactions between the monsoon flow and the orography north of major coastal

834   cities as well as the land-sea and land-lake breezes, and their impact on the

835   dispersion of pollution emissions form major coastal cities in SWA. Future research will

836   also be conducted to assess long-term impact of the land-sea surface temperature

837   gradient (and related shallow overturning circulation) on distribution of aerosols over

838   the northern Gulf of Guinea.

839

855   Sophie Haslett and Johnathan Taylor (Univ. of Manchester) for helpful discussions.

856   MODIS data was made available via the Geospatial Interactive Online Visualization

857   ANd aNalysis interface (https://giovanni.gsfc.nasa.gov/giovanni/).

858

859   **Data availability**

860

861   The aircraft and radiosonde data used here can be accessed using the DACCIWA

862   database at http://baobab.sedoo.fr/DACCIWA/. The tracer simulations discussed in

863   this paper are also available on the database. An embargo period of 2 years after

864   the upload applies. After that, external users can access the data in the same way

865   as DACCIWA participants before that time. Before the end of the embargo period,

866   external users can request the release of individual datasets. It is planned for

867   DACCIWA data to get DOIs, but this has not been realized for all datasets yet.

868

869

870   **Competing interests**

871

872   The authors declare that they have no conflict of interest.

873

874   **Special issue statement**

875

876   This article is part of the special issue "Results of the project 'Dynamics-aerosol-

877   chemistry-cloud interactions in West Africa' (DACCIWA) (ACP/AMT inter-journal SI)". It

878   is not associated with a conference.

879

880

881   **Appendix A: The ULICE lidar characteristics and data processing**

882

883   For the two channels of the lidar (indexed 1 and 2), the apparent backscatter

884   coefficient (ABC, β_{app}) is given by

885     $$\beta_{app}^{1(2)}(r) = C^{1(2)} \cdot \left(\beta_m^{1(2)}(r) + \beta_a^{1(2)}(r) \right) \cdot \exp\left(-2 \cdot \int_0^r \alpha_a(r') \cdot dr' \right) \qquad (A1)$$

886   where β_m and β_p are the backscatter coefficients for the molecular and the aerosol

887   contributions, respectively; α_a is the aerosol extinction coefficient; $C^{1(2)}$ are the

888   instrumental constants for each channel. The total ABC is given by:

889     $$\beta_{app}(r) = \frac{\beta_{app}^1(r) \cdot (1 + VDR(r))}{C^1 \cdot \left(T_1^{//} + T_1^{\perp} \cdot VDR(r) \right)} \qquad (A2)$$

890   where $T_i^{//}$ and $T_i^{\perp}$ are the transmissions of the co-polarization and cross-polarization

891   contributions of the lidar polarized plate i, respectively. The VDR is thus given by the

892   equation:

893     $$VDR(r) \approx \frac{T_1^{//} \cdot \beta_{app}^2(r)(r)}{R_c \cdot \beta_{app}^1(r)(r)} - \left(1 - T_1^{//} \right) \cdot \left(1 - T_2^{//} \right). \qquad (A3)$$

894   The apparent scattering ratio (ASR, noted R_{app}) is expressed as:

895     $R_{app}(r) = \beta_{app}(r) / \beta_m^{//}(r).$ \qquad (A4)

896

897   As also shown by Chazette et al. (2012), the cross-calibration coefficient $R_c = C^2/C^1$

898   can be assessed by normalizing the lidar signals obtained in aerosol-free conditions,

899   assuming the molecular VDR to be equal to 0.3945% at 355 nm, following Collis and

900   Russel (1976). The dominant error source is the characterization of the plate

901   transmission on the optical bench, which leads to a relative error close to 8% on the

902   VDR (Chazette et al., 2012). During the DACCIWA field campaign, all lidar

Atmospheric
Chemistry
and Physics
Discussions

903   measurements were conducted within aerosol layers and therefore we had to use

904   measurements performed just before the campaign during flight tests above the

905   Mediterranean Sea for assessing R_c.

906

907

Atmospheric
Chemistry
and Physics
Discussions

908   Table A1. Summary of ULICE lidar characteristics

ULICE lidar	Characteristics
Emitter (Laser)	Quantel Centurion, diode-pumped, air cooled
	6.5 mJ, 8 ns, 100 Hz @ 354.7 nm
Laser divergence	< 0.1 mrad
Output beam	Eyesafe ~40 × 30 mm beam, tunable 0 to 40 mrad divergence
	with Altechna Motex expander (at $1/e^2$)
Receiver	2 channels with the cross-polarisations
Telescope	Refractive,150 mm diameter, 280 mm effective focal length
Field of view	~3 mrad
Filtering	Narrow band filters (200 pm)
Detection	Hamamatsu H10721 photo-multiplier tubes.
Detection mode	Analog
Data acquisition	12 bits, 200 MHz sampling, 2 channels NI-5124 digitizer manufactured by the National Instruments Company.
Vertical sampling	
Native	0.75 m
After data processing	15-30 m
Weight of the optical head	~20 kg
Weight of the electronics	~10 kg
Consumption	350 W at 24-28 V DC

909

910

911

912

913

Atmospheric
Chemistry
and Physics
Discussions

Open Access

EGU

914 **References**

915

916 Anderson, T. L. and Ogren, J. A., 1998: Determining aerosol radiative properties using

917   the TSI 3563 integrating nephelometer, Aerosol Sci. Tech., 29, 57–69.

918

919 Bennouna, Y. S., G. de Leeuw, J. Piazzola, and J. Kusmierczyk-Michulec (2009),

920   Aerosol remote sensing over the ocean using MSG-SEVIRI visible images, J.

921   Geophys. Res., 114(D23), D23203, doi:10.1029/2008JD011615.

922

923 Bergstrom, R. W., Pilewskie, P., Russell, P. B., Redemann, J., Bond, T. C., Quinn, P. K.,

924   and Sierau, B.: Spectral absorption properties of atmospheric aerosols, Atmos.

925   Chem. Phys., 7, 5937-5943, https://doi.org/10.5194/acp-7-5937-2007, 2007.

926

927 Bond, T. C., Anderson, T. L., and Campbell, D., 1999: Calibration and intercomparison

928   of filter-based measurements of visible light absorption by aerosols, Aerosol Sci.

929   Tech., 30, 582–600.

930

931 Brito, J., E. Freney, P. Dominutti, A. Borbon, S. Haslett, A. Batenburg, C. Schulz, A.

932   Colomb, R. Dupuy, C. Denjean, A. Deroubaix, H. Coe, J. Schneider, S. Borrmann,

933   K. Sellegri, C. Flamant, P. Knippertz and A. Schwarzenboeck, 2018: Assessing the

934   role of anthropogenic and biogenic sources on PM1 over Southern West Africa

935   using aircraft measurements, *Atmos. Chem. Phys.* 18, 757–772.

936

937 Buchholz M., A. H. Fink, P. Knippertz, and C. Yorke, 2017a: Impacts of the land-lake

938   breeze of the Volta reservoir on the diurnal cycle of cloudiness and

939   precipitation, EGU General Assembly, Vienna, Austria, 23-28 April 2017.

Atmospheric
Chemistry
and Physics
Discussions

Open Access

EGU

940

941   Buchholz M. A., 2017b: The influence of Lake Volta on weather and climate, Karlsruhe

942   Institute   of   Technology   Master   Thesis   (in   German),   available   from

943   http://www.imk-tro.kit.edu/download/Masterarbeit_Marcel_Buchholz.pdf

944

945   Burton, S. P., J. W. Hair, M. Kahnert, R. A. Ferrare, C. A. Hostetler, A. L. Cook, D. B.

946   Harper, T. A. Berkoff, S. T. Seaman, J. E. Collins, M. A. Fenn, and R. R. Rogers, 2015:

947   Observations of the spectral dependence of linear particle depolarization ratio

948   of aerosols using NASA Langley airborne High Spectral Resolution Lidar, Atmos.

949   Chem. Phys., 15(23), 13453–13473, doi:10.5194/acp-15-13453-2015.

950

951   Carslaw, K. S., Boucher, O., Spracklen, D. V., Mann, G. W., Rae, J. G. L., Woodward,

952   S., and Kulmala, M.: A review of natural aerosol interactions and feedbacks

953   within the Earth system, Atmos. Chem. Phys., 10, 1701-1737, doi:10.5194/acp-10-

954   1701-2010, 2010.

955

956   Clarke, A., McNaughton, C., Kapustin, V., Shinozuka, Y., Howell, S., Dibb, J., Zhou, J.,

957   Anderson, B., Brekhovskikh, V., Turner, H., and Pinkerton, M., 207: Biomass Burning

958   and Pollution Aerosol over North America: Organic Components and their

959   influence on Spectral Optical Properties and Humidification Response, J.

960   Geophys. Res., 112, D12S18, doi:10.1029/2006JD007777.

961

962   Chazette, P., A. Dabas, J. Sanak, M. Lardier, and P. Royer, 2012: French airborne lidar

963   measurements for Eyjafjallajökull ash plume survey, Atmos. Chem. Phys., 12(15),

964   7059–7072, doi:10.5194/acp-12-7059-2012.

965   Collaud Coen, M., Weingartner, E., Schaub, D., Hueglin, C., Corrigan, C., Henning, S.,

Atmospheric
Chemistry
and Physics
Discussions

966   Schikowski, M., and Baltensperger, U., 2004: Saharan dust events at the

967   Jungfraujoch: Detection by wavelength dependence of the single scattering

968   albedo and first climatology analysis, Atmos. Chem. Phys., 4, 2465–2480.

969

970   Collis, R. T. H. and P. B. Russell,1976: Lidar measurement of particles and gases by

971   elastic backscattering and differential absorption in Laser Monitoring of the

972   Atmosphere, edited by: Hinkley, E. D., pp. 71–152, Springler-Verlag, New York.

973

974   Deroubaix, A., Flamant, C., Menut, L., Siour, G., Mailler, S., Turquety, S., Briant, R.,

975   Khvorostyanov, D., and Crumeyrolle, S., 2018: Interactions of Atmospheric Gases

976   and Aerosols with the Monsoon Dynamics over the Sudano-Guinean region

977   during AMMA, Atmos. Chem. Phys., doi:10.5194/acp-2017-552, accepted

978

979   Evan, A. T., Vimont, D. J., Heidinger, A. K., Kossin, J. P. & Bennartz, R., 2009: The role of

980   aerosols in the evolution of tropical North Atlantic Ocean temperature

981   anomalies. Science 324, 778–781.

982

983   Flamant C., P. Knippertz, A. H. Fink, A. Akpo, B. Brooks, C. J. Chiu, H. Coe, S. Danuor,

984   M. Evans, O. Jegede, N. Kalthoff, A. Konaré, C. Liousse, F. Lohou, C. Mari, H.

985   Schlager, A. Schwarzenboeck, B. Adler, L. Amekudzi, J. Aryee, M. Ayoola, A. M.

986   Batenburg, G. Bessardon, S. Borrmann, J. Brito, K. Bower, F. Burnet, V. Catoire, A.

987   Colomb, C. Denjean, K. Fosu-Amankwah, P. G. Hill, J. Lee, M. Lothon, M.

988   Maranan, J. Marsham, R. Meynadier, J.-B. Ngamini, P. Rosenberg, D. Sauer, V.

989   Smith, G. Stratmann, J. W. Taylor, C. Voigt, and V. Yoboué, 2018 : The Dynamics-

990   Aerosol-Chemistry-Cloud Interactions in West Africa field campaign: Overview

991   and research highlights, Bull. Amer. Meteorol. Soc., 99, 83-104, doi:10.1175/BAMS-

Atmospheric
Chemistry
and Physics
Discussions

992   D-16-0256.1.

993

994   Flemming, J., Huijnen, V., Arteta, J., Bechtold, P., Beljaars, A. Blechschmidt, A.-M.,

995   Diamantakis, M., Engelen, R. J., Gaudel, A., Inness, A., Jones, L., Josse, B.,

996   Katragkou, E., Marecal, V., Peuch, V.-H., Richter, A., Schultz, M. G., Stein, O., and

997   Tsikerdekis, A., 2015: Tropospheric chemistry in the Integrated Forecasting System

998   of ECMWF, Geosci. Model Dev., 8, 975-1003, doi:10.5194/gmd-8-975-2015.

999

1000   Haywood, J. and Boucher, O.: Estimates of the direct and indirect radiative forcing

1001   due to tropospheric aerosols: A review, Rev. Geophys., 38, 513–543, 2000.

1002

1003   Huang, J., C. Zhang and J. M. Prospero, 2009: Large-scale effect of aerosols on

1004   precipitation in the West African Monsoon region Q. J. R. Meteorol. Soc., 135,

1005   581–594, doi:10.1002/qj.391.

1006

1007   King, M. D., Y. J. Kaufman, W. P. Menzel, and D. Tanré, Remote-sensing of cloud,

1008   aerosol, and water-vapor properties from the Moderate Resolution Imaging

1009   Spectrometer (MODIS), IEEE Trans. Geosci. Remote Sens., 30(1), 2–27, 1992.

1010

1011   Kalthoff, N., Lohou, F., Brooks, B., Jegede, G., Adler, B., Babić, K., Dione, C., Ajao, A.,

1012   Amekudzi, L. K., Aryee, J. N. A., Ayoola, M., Bessardon, G., Danuor, S. K.,

1013   Handwerker, J., Kohler, M., Lothon, M., Pedruzo-Bagazgoitia, X., Smith, V.,

1014   Sunmonu, L., Wieser, A., Fink, A. H., and Knippertz, P., 2018: An overview of the

1015   diurnal cycle of the atmospheric boundary layer during the West African

1016   monsoon season: Results from the 2016 observational campaign, accepted in

1017   Atmos. Chem. Phys., https://doi.org/10.5194/acp-2017-631

Atmospheric
Chemistry
and Physics
Discussions

1018

1019 Knippertz, P., A. H. Fink, A. Deroubaix, E. Morris, F. Tocquer, M. Evans, C. Flamant, M.

1020 Gaetani, C. Lavaysse, C. Mari, J. H. Marsham, R. Meynadier, A. Affo-Dogo, T.

1021 Bahaga, F. Brosse, K. Deetz, R. Guebsi, I. Latifou, M. Maranan, P. D. Rosenberg,

1022 and A. Schlueter, 2017: A meteorological and chemical overview of the

1023 DACCIWA field campaign in West Africa in June–July 2016, *Atmos. Chem. Phys.*

1024 *Disc.*, doi:10.5194/acp-2017-345

1025

1026 Knippertz, P., M. Evans, P. R. Field, A. H. Fink, C. Liousse, and J. H. Marsham, 2015a: The

1027 possible role of local air pollution in climate change in West Africa. *Nature Clim.*

1028 *Change,* doi:10.1038/NCLIMATE2727.

1029

1030 Knippertz P., H. Coe, C. Chiu, M. J. Evans, A. H. Fink, N. Kalthoff, C. Liousse, C. Mari, R.

1031 Allan, B. Brooks, S. Danour, C. Flamant, O. O. Jegede, F. Lohou and J. H.

1032 Marsham, 2015b: The DACCIWA project: Dynamics-aerosol-chemistry-cloud

1033 interactions in West Africa, *Bull. Amer. Meteorol. Soc.*, **96,** 1451-1460.

1034

1035 Lelieveld J., J. S. Evans, M. Fnais, D. Giannadaki and A. Pozzer, 2015: The contribution

1036 of outdoor air pollution sources to premature mortality on a global scale, *Nature,*

1037 525, 367-371.

1038

1039 Liousse, C., Assamoi, E., Criqui, E. P., Granier, C. & Rosset, R., 2014: Explosive growth in

1040 African combustion emissions from 2005 to 2030. *Environ. Res. Lett.* **9,** 035003.

1041

1042 Lothon M, Said F, Lohou F, Campistron B. 2008. Observation of the diurnal cycle in the

1043 low troposphere of West Africa. *Mon. Weather Rev.* **136**: 3477–3500.

Atmospheric
Chemistry
and Physics
Discussions

Open Access

1044

1045   Mailler S., L. Menut, A. G. Di Sarra, S. Becagli, T. Di Iorio, B. Bessagnet, R. Briant, P.

1046   Formenti, J.F. Doussin, J. L. Gomez-Amo, M. Mallet, G. Rea, G. Siour, D. M.

1047   Sferlazzo, R. Traversi, R. Udisti, and S. Turquety, 2016: On the radiative impact of

1048   aerosols on photolysis rates: comparison of simulations and observations in the

1049   Lampedusa island during the CharMEx/ADRIMED campaign, Atmos. Chem.

1050   Phys., 16, 1219-1244, doi:10.5194/acp-16-1219-2016.

1051

1052   Mailler S., L. Menut, D. Khvorostyanov, M. Valari, F. Couvidat, G. Siour, S. Turquety, R.

1053   Briant, P. Tuccella, B. Bessagnet, A. Colette, L. Letinois, and F. Meleux, 2017:

1054   CHIMERE-2017: from urban to hemispheric chemistry-transport modeling ,

1055   Geosci. Model Dev., 10, 2397-2423, doi:10.5194/gmd-10-2397-2017.

1056

1057   Paola Massoli , Paul L. Kebabian , Timothy B. Onasch , Frank B. Hills& Andrew

1058   Freedman (2010) Aerosol Light Extinction Measurements by Cavity Attenuated

1059   Phase Shift (CAPS) Spectroscopy: Laboratory Validation and Field Deployment

1060   of a Compact Aerosol Particle Extinction Monitor, Aerosol Science and

1061   Technology, 44:6, 428-435, DOI:10.1080/02786821003716599

1062

1063   Menut, L., C. Flamant, S. Turquety, A. Deroubaix, P. Chazette and R. Meynadier, 2018:

1064   Impact of biomass burning on pollutants surface concentrations in megacities of

1065   the Gulf of Guinea, *Atmos. Chem. Phys.* accepted.

1066

1067   Müller, T., Nowak, A., Wiedensohler, A., Sheridan, P., Laborde, M., Covert, D. S.,

1068   Marinoni, A., Imre, K., Henzing, B., Roger, J.-C., Martins dos Santos, S., Wilhelm, R.,

1069   Wang, Y.-Q. and de Leeuw, G., 2009: Angular Illumination and Truncation of

Atmospheric
Chemistry
and Physics
Discussions

1070   Three Different Integrating Nephelometers: Implications for Empirical, Size-Based

1071   Corrections, Aerosol Sci. Tech., 43(43), 581–586.

1072

1073   Müller, T., J. S. Henzing, G. De Leeuw, A. Wiedensohler, A. Alastuey, et al., 2011:

1074   Characterization and intercomparison of aerosol absorption photometers: result

1075   of two intercomparison workshops, Atmos. Meas. Tech., 4, 245-268.

1076

1077   Parker, D. J., Kassimou, A., Orji, B. N., Osika, D. P., Hamza, I., Diop-Kane, M., Fink, A.,

1078   Galvin, J., Guichard, F., Lamptey, B. L., Hamidou, H., van der Linden, R., Redl, R.,

1079   Lebel, T. and Tubbs, C., 2017: Local Weather, in Meteorology of Tropical West

1080   Africa: The Forecasters' Handbook (eds D. J. Parker and M. Diop-Kane), John

1081   Wiley & Sons, Ltd, Chichester, UK. doi: 10.1002/9781118391297.ch4

1082

1083   Parker DJ, Burton RR, Diongue-Niang A, Ellis RJ, Felton MA, Taylor CM, Thorncroft CD,

1084   Bessemoulin P, Tompkins A., 2005: The diurnal cycle of the West African Monsoon

1085   circulation. *Q. J. R. Meteorol. Soc.* **131**: 2839–2860.

1086

1087   Remer, L.A., Kaufman, Y.J., Tanré, D., Mattoo, S., Chu, D.A., Martins, J. V., Li, R.-R.,

1088   Ichoku, C., Levy, R.C., Kleidman, R.G., Eck, T.F., Vermote, E., Holben, B.N., 2005.

1089   The MODIS Aerosol Algorithm, Products, and Validation. J. Atmos. Sci. 62, 947–

1090   973. doi:10.1175/JAS3385.1

1091

1092   Shamarock, W.C. and J.B. Klemp, 2008: A time-split nonhydrostatic atmospheric

1093   model for weather research and forecasting applications, Journal of

1094   Computational Physics 227 (2008) 3465–3485.

1095

1096   Shang, X. and Chazette, P. (2014), Interest of a Full-Waveform Flown UV Lidar to

1097   Derive Forest Vertical Structures and Aboveground Carbon, Forests, 5, 1454-1480;

1098   doi:10.3390/f5061454.

1099

1100   Thiébaux, J., E. Rogers, W. Wang and B. Katz, 2003: A new high-resolution blended

1101   real-time global sea surface temperature analysis, Bull. Amer. Meteorol. Soc., 84,

1102   645-656, doi:10.1175/BAMS-84-5-645.

1103

1104   Werdell, P.J., B.A. Franz, S.W. Bailey, G.C. Feldman and 15 co-authors, 2013:

1105   Generalized ocean color inversion model for retrieving marine inherent optical

1106   properties, Applied Optics 52, 2019-2037.

1107

1108   Winker, D. M., W. H. Hunt, and M. J. McGill (2007), Initial performance assessment of

1109   CALIOP, Geophys. Res. Lett., 34(19), doi:10.1029/2007GL030135.

1110

1111   World Urbanization Prospects: The 2014 Revision, United Nations, Department of

1112   Economic and Social Affairs, Population Division, 2015, ST/ESA/SER.A/366, Pp 517,

1113   http://www.un.org/en/development/desa/population/publications/pdf/urbaniz

1114   ation/WUP2011_Report.pdf

1115

1116   Zhang, Y., R. Fu, H. Yu, R. E. Dickinson, R. N. Juarez, M. Chin, and H. Wang, 2008: A

1117   regional climate model study of how biomass burning aerosol impacts land-

1118   atmosphere interactions over the Amazon, J. Geophys. Res., 113, D14S15,

1119   doi:10.1029/2007JD009449.

1120

Atmospheric
Chemistry
and Physics
Discussions

1121   Zhang, Y., R. Fu, H. Yu, Y. Qian, R. Dickinson, M. A. F. Silva Dias, P. L. da Silva Dias, *and*

1122   K. Fernandes, 2009: Impact of biomass burning aerosol on the monsoon

1123   circulation transition over Amazonia, Geophys. Res. Lett., 36, *L10814,*

1124   *doi:*10.1029/2009GL037180.

1125

1126

1127

1128 **Tables**

1129

1130 Table 1. SAFIRE ATR 42 payload. Only instruments used in this study are listed. The

1131 complete payload is detailed in Flamant et al. (2018).

Instrument	Parameter	Responsible institution
P (static & dynamic): Rosemount 120 & 1221	Pressure	SAFIRE / CNRS
INS + GPS inertial units	Wind component, position	SAFIRE / CNRS
Adjustable (flow, orientation) Aerosol Community Inlet	Particle aerosol sampling D50 = 5 µm	CNRM / CNRS
Aircraft DUAL CPC counter MARIE	Particle number concentrations D>4 nm & D>15 nm (variable) 1 s time resolution	LaMP / UBP
OPC Grimm 1.109	Ambient particle size distribution 0.25–25 µm 6 s time resolution	CNRM / CNRS
PSAP (3λ)	Absorption coefficient, black carbon content Blue 476 nm, green 530 nm, red 660 nm	LaMP / UPB
CAPS	Extinction Mm^{-1} 530 nm 1 s time resolution	CNRM / CNRS
Mozart	CO, O_3 measured every second, then averaged over 30 s O_3: 1 ppbv; CO: 5 ppbv	SAFIRE / CNRS
TEI 42CTL NOx analyser	NOx; measured every 1 s, then	SAFIRE / CNRS

	averaged over n x 10s 50ppt integration over 120 s	
PICARRO	CO_2, CH_4, CO cavity ring down spectroscopy carbon dioxide (CO_2) every 5s with precision 150 ppb; methane (CH_4) 1 ppb, and CO to a precision of 30 ppb	SAFIRE / CNRS
ULICE Aerosol / cloud lidar	Aerosol backscatter @ 355 nm	LSCE / UPMC

1132

1133

Atmospheric
Chemistry
and Physics
Discussions

1134   Table 2. Correlation between vertical velocity and land-sea skin temperature

1135   gradients at 0000, 0600, 1200 and 1800 UTC for July 2016. The land-sea zonal skin

1136   temperature gradient is computed using a 'land box' defined as 6–9°E and 4.5–6.5°N

1137   and a 'sea box' defined as 2–5°E and 4.5–6.5°N. The land-sea meridional skin

1138   temperature gradient is computed using a 'land box' defined as 2°W–2°E and 6–8°N

1139   and a 'sea box' defined as 2°W–2°E and 3–5°N. Vertical velocity is averaged in the

1140   layer 850–600 hPa over a box defined as 2°W–2°E and 4–6°N. Correlations are

1141   computed using vertical velocity and skin temperature gradient indices standardized

1142   to 0000, 0600, 1200 and 1800 UTC means for the month of July 2016. Significant

1143   correlations (and their p values) are given in bold.

1144

Zonal cell		Vertical velocity			
		0000 UTC	0600 UTC	1200 UTC	1800 UTC
Skin temperature gradient	0000 UTC	0.26	-0.04	0.12	-0.17
	0600 UTC		-0.08	0.09	0.11
	1200 UTC			0.02	**0.53 (p=0.002)**
	1800 UTC				**0.46 (p=0.01)**
Meridional cell		Vertical velocity			
		0000 UTC	0600 UTC	1200 UTC	1800 UTC
Skin temperature gradient	0000 UTC	0.07	-0.22	0.06	-0.07
	0600 UTC		-0.01	0.01	-0.06
	1200 UTC			**0.34 (p=0.06)**	-0.24

Atmospheric
Chemistry
and Physics
Discussions

	1800 UTC				0.20

1146

1147

Figures

1149

(a)

(b)
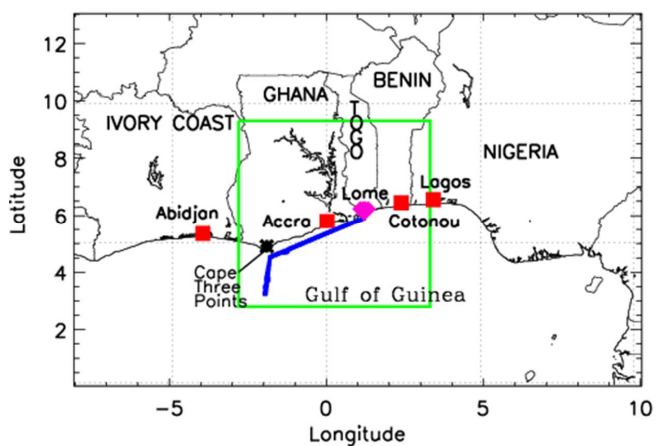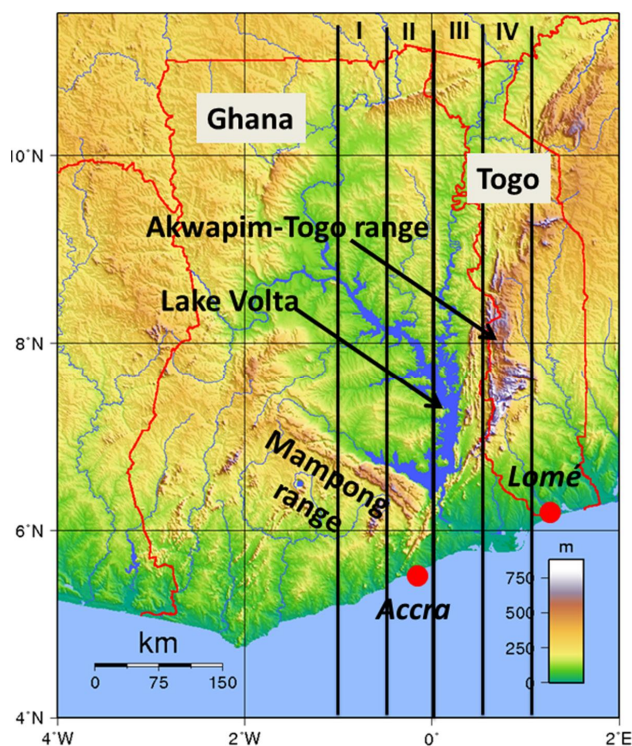
Figure 1: (a) Map of southern West Africa with the location of the main landmarks (e.g. cities, countries). The thick blue line represents the ATR 42 flight track in the afternoon of 2 July 2016. The red filled square symbols represent DACCIWA radiosounding stations used in this study. The pink filled circle represents the base of operation for aircraft during the DACCIWA field campaign. The green thick box represents the domain of the 2-km WRF simulation. (b) Topographic map of Ghana and Togo showing the main features of interest for this study as well as the transects along which tracer simulations are shown in **Figure 8**. The transects are centered at 0.75°W, 0.25°W, 0.25°E and 0.75°E (for I, II, III and IV, respectively) and are 0.5° wide.

(a)

(b)

1160
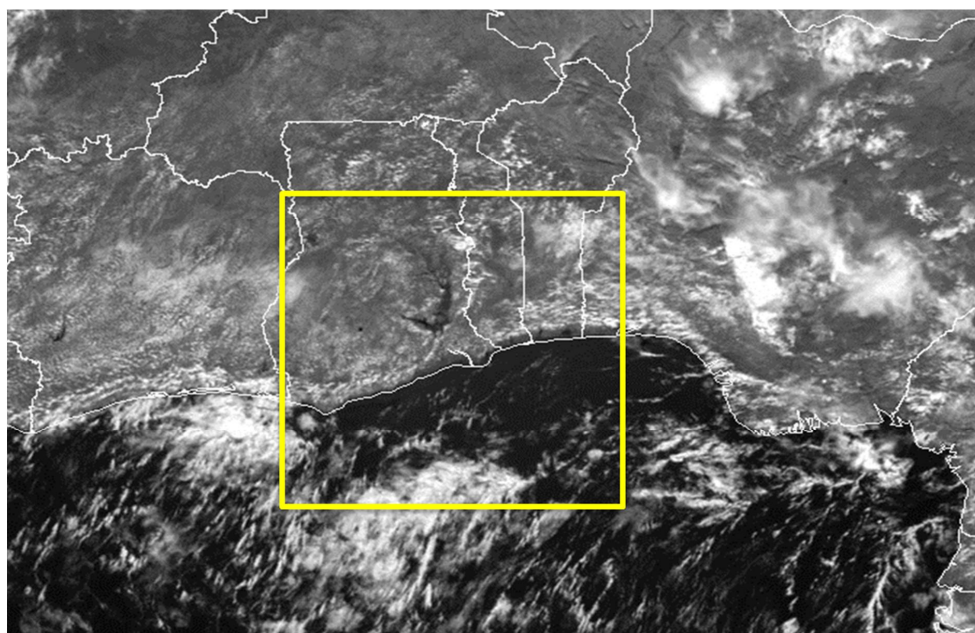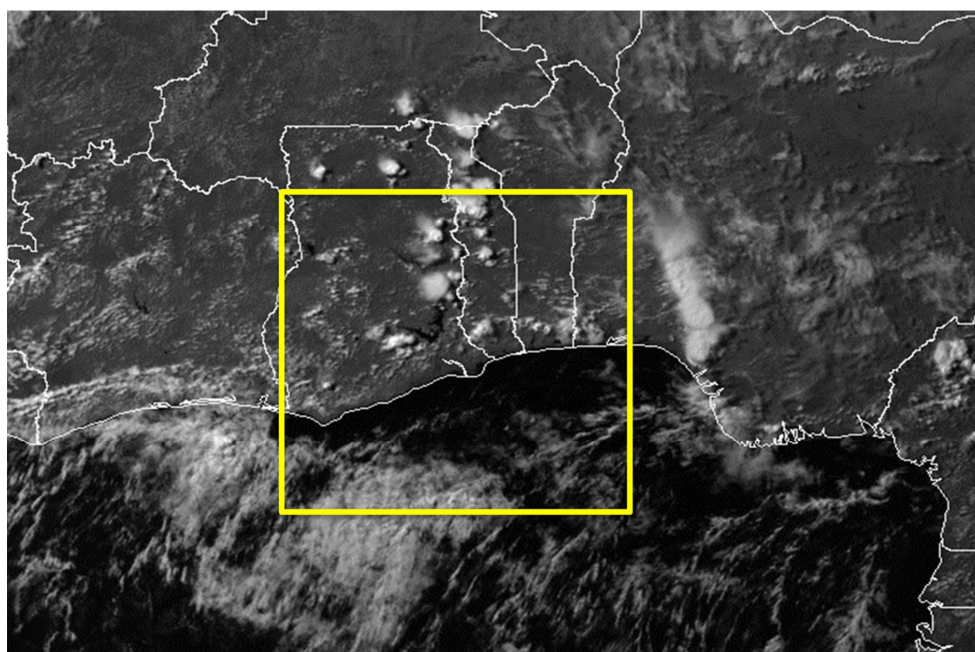
1161   Figure 2: SEVIRI visible images of SWA on 2 July at (a) 1200 UTC and (b) 1500 UTC.

1162   Country borders are shown as solid white lines. The yellow thick box represents the

1163   domain of the 2-km WRF simulation as in **Figure 1a**.

1164

1165
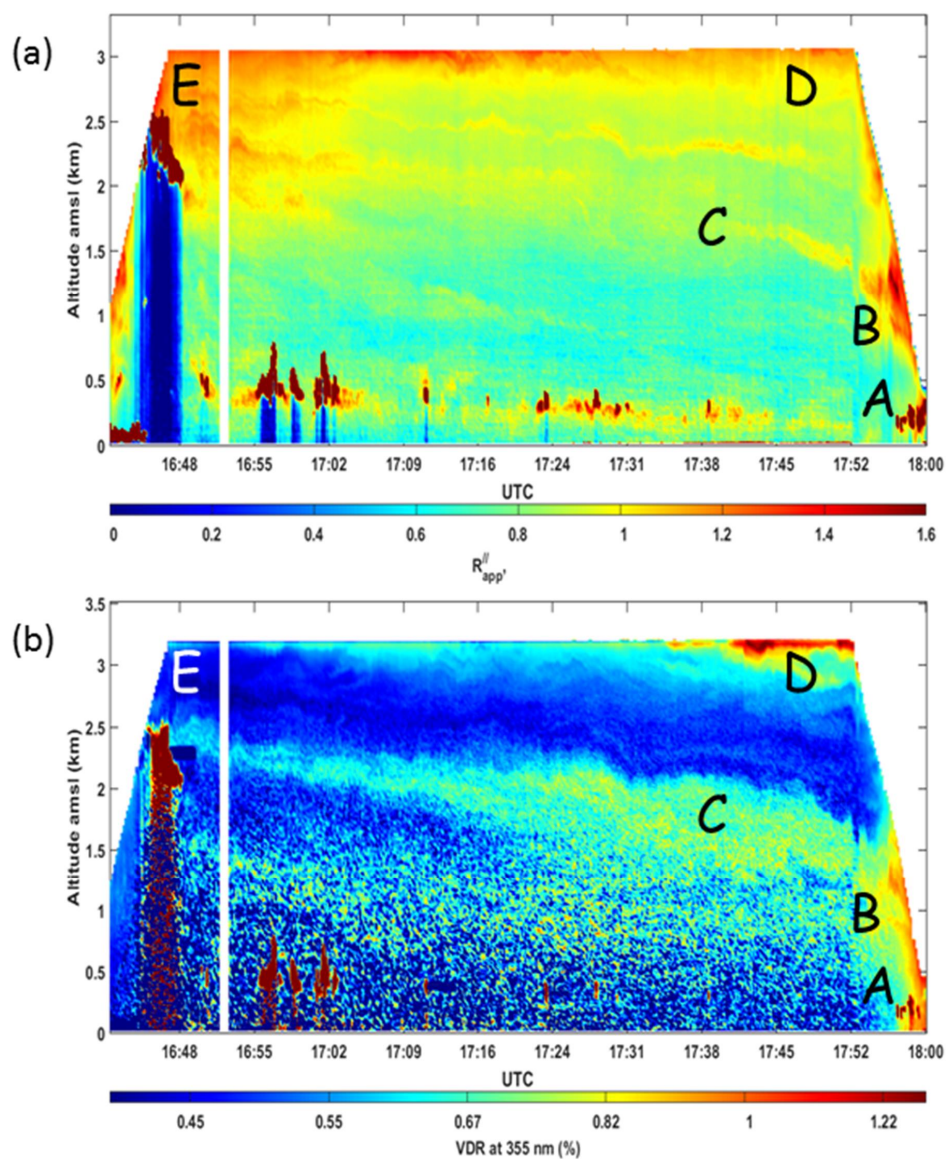
1166

Figure 3: Time-height evolution of ULICE-derived (a) apparent scattering ratio (R_{app})

and (b) volume depolarization ratio (VDR) below the ATR 42 flight track over the Gulf

of Guinea between 1644 and 1800 UTC on 2 July 2016 (see **Figure 1a**). The ATR leg

Atmospheric
Chemistry
and Physics
Discussions

1170   parallel to the coastline starts at 1654 UTC. The ATR passed the longitude of Accra at

1171   1729 UTC. See text for explanations of features A–E.

1172

1173
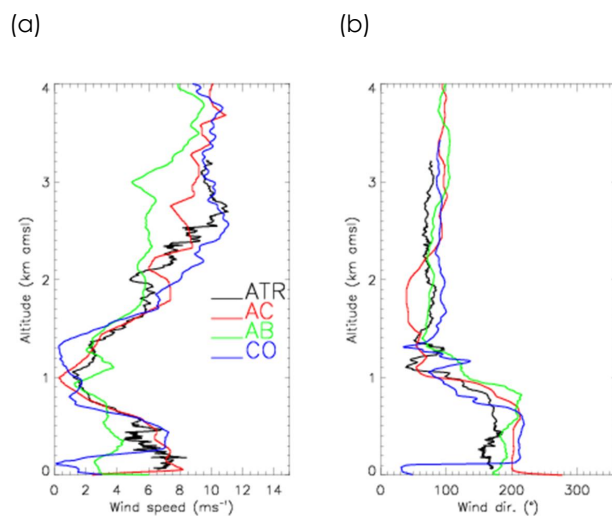
1174

Figure 4: (a) Wind speed and (b) wind direction profiles measured during the ATR 42

sounding over the ocean (1630 to 1647 UTC, ATR, black solid line) as well as from the

radiosoundings launched in Accra at 1700 UTC (AC, red solid line), in Abidjan at 1608

UTC (AB, green solid line) and in Cotonou at 1612 UTC (CO, blue solid line). The

location of the radiosounding sites is shown in **Figure 1a**.

1180

1181

Atmospheric
Chemistry
and Physics
Discussions

(g)
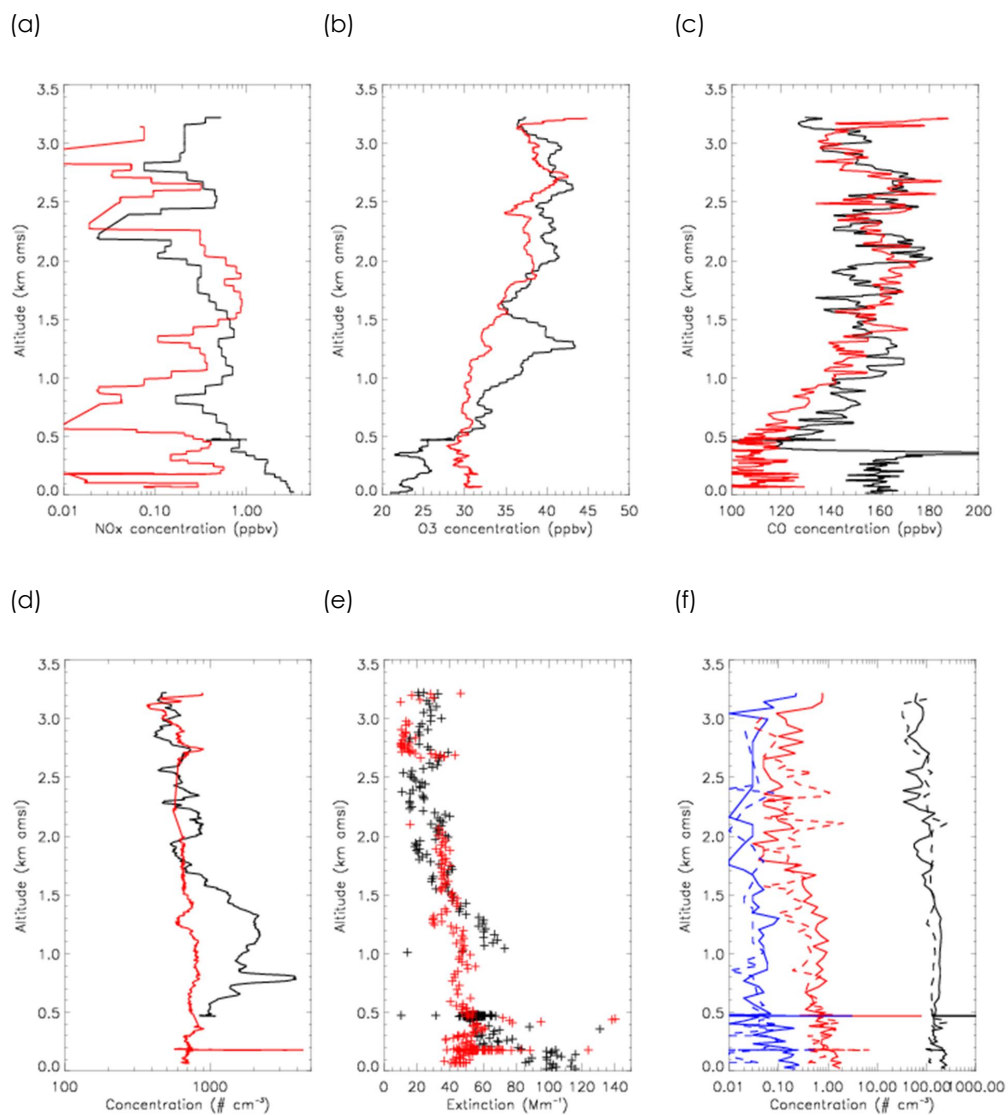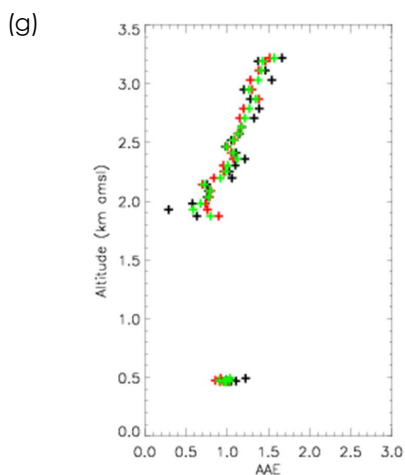
Figure 5: Profiles measured during the ATR 42 sounding over the ocean (1633 to 1647 UTC, red solid line) and at the coast in the vicinity of Lomé (1753 to 1807 UTC, black solid line) for (a) NO_x concentration, (b) O_3 concentration, (c) CO concentration, (d) total aerosol concentration N_{10} measured with the CPC and (e) extinction coefficient. (f) N_{PM1}, $N_{PM2.5}$ and N_{PM10} concentration profiles (black, red and blue, respectively) measured over the ocean (dashed lines) and at the coast in the vicinity of Lomé (solid lines). (g) AAE profiles in the vicinity of Lomé computed between 467 and 530 nm, 530 and 660 nm, and 467 and 660 nm (black, red and green solid symbols, respectively).

1192
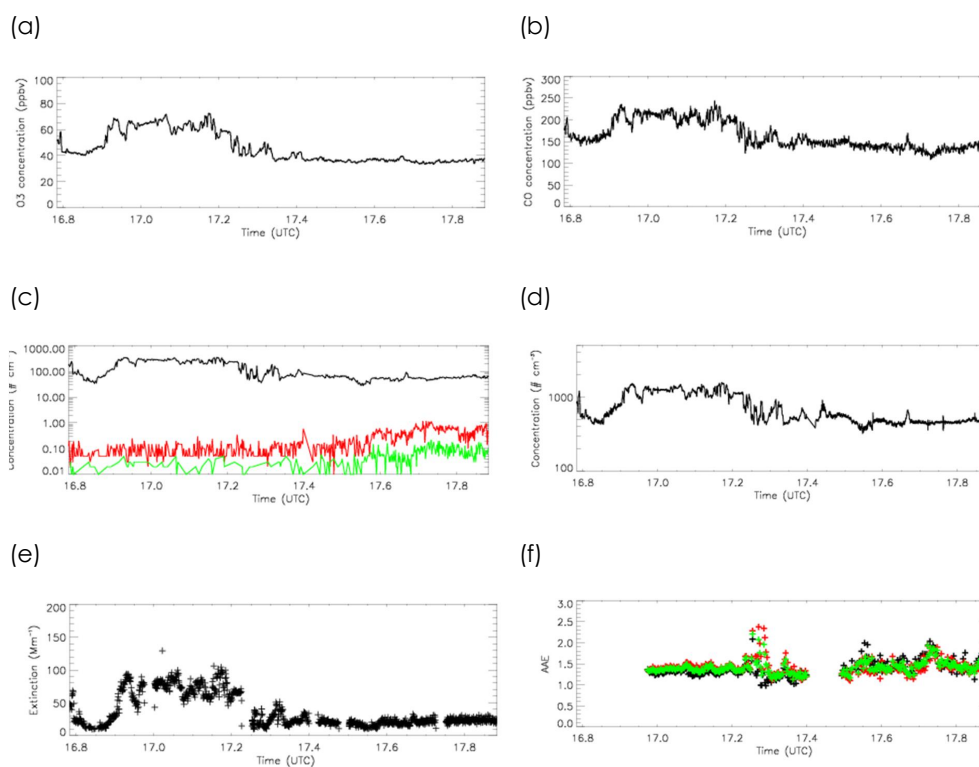
Figure 6: (a) O_3 concentration, (b) CO concentration, (c) N_{PM1}, $N_{PM2.5}$ and N_{PM10} concentrations (black, red and green, respectively), (d) CPC-derived total aerosol concentration N_{10}, (e) extinction coefficient and (f) AAE computed between 476 and 530 nm, 530 and 660 nm, and 476 and 660 nm (black, red and green crosses, respectively) measured during the ATR 42 elevated straight level run from 1647 to 1753 UTC.

1199

1200

(a)

(b)

(c)

(d)
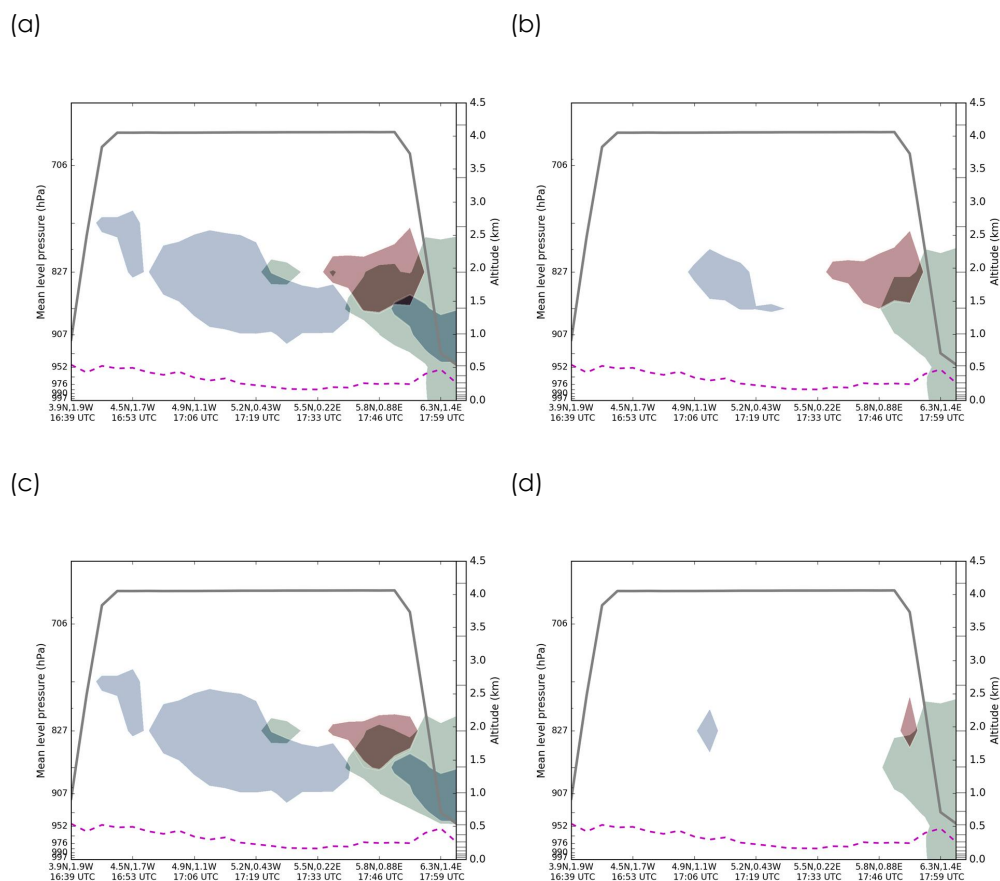
Figure 7: Time-height evolution of tracer concentration (a.u.) below the ATR 42 between 1400 and 1800 UTC for (a) the TRA_D1, (b) TRA_I1, (c) TRA_D2 and (d) TRA_D3 experiments (see section 3.2.1 for details). Tracer emissions in Accra, Lomé and Cotonou appear in blueish, greenish and reddish colors, respectively. The solid grey line represents the altitude of the aircraft. The dashed blue line represents the height of the top of the marine ABL from the WRF 2-km simulation.

1208

(a)   (b)

(c)   (d)
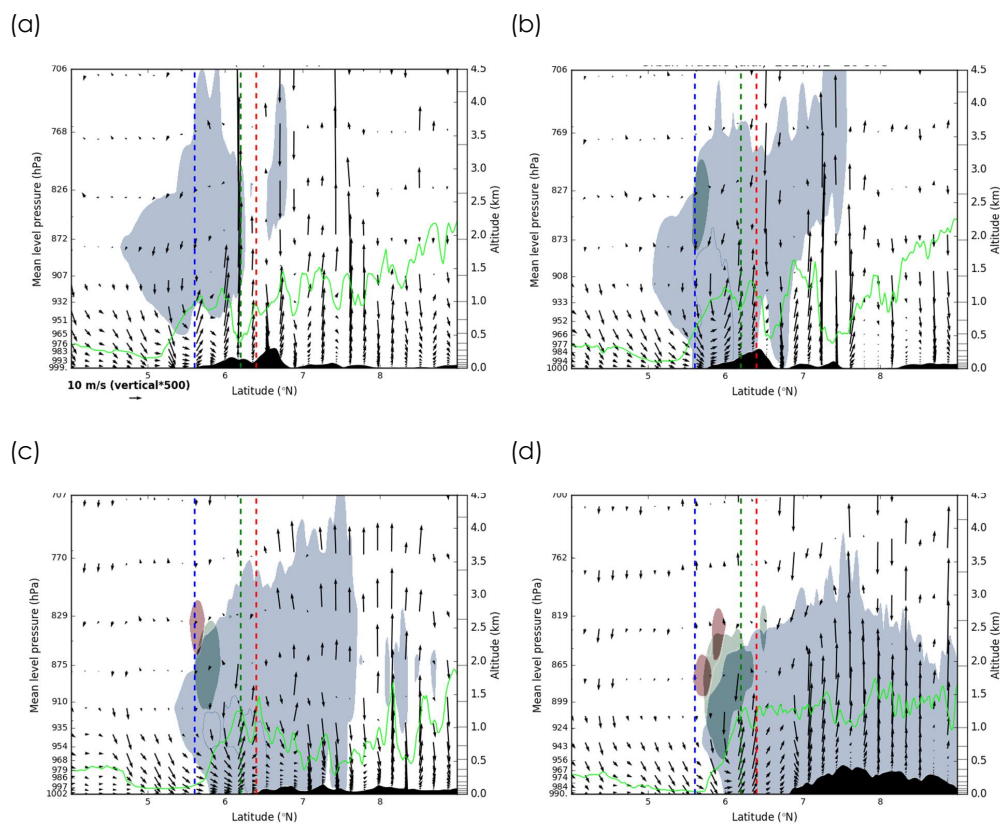
Figure 8: Tracer concentrations (a.u.) from the TRA_D1 experiment (see section 3.2.1 for details) along four 0.5°-wide north–south transects centered on (a) 0.75°W, (b) 0.25°W, (c) 0.25°E and (d) 0.75°E (marked I, II, III and IV, respectively, in **Figure 1b**) at 1600 UTC. Tracer emissions in Accra, Lomé and Cotonou appear in blueish, greenish and reddish colors, respectively, as in **Figure 7**. Also shown are meridional-vertical wind vectors in the transects. The green solid line represents the ABL derived from the WRF 2-km simulation. The vertical dashed lines represent the location of the cities of Accra (blue), Lomé (green) and Cotonou (red). The orography along the transects is shaded in black.

1218

(a)

(b)
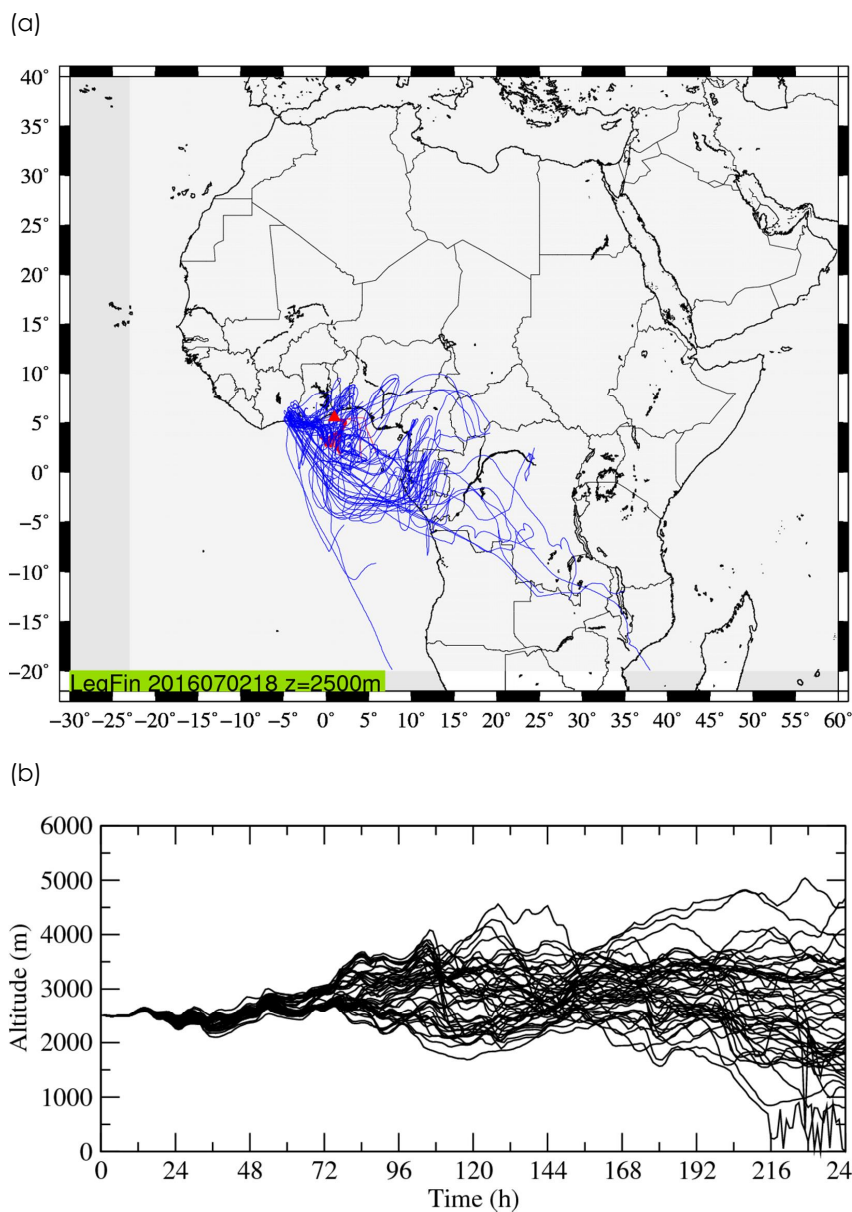
1219

Figure 9: 10-day CHIMERE-derived backplume ending at 2500 m amsl at 5.5°N/1°E at

1700 UTC on 2 July 2016. (a) Individual trajectories are shown as blue solid lines over

a political map of Africa with state borders appearing in black. The red triangle

Atmospheric
Chemistry
and Physics
Discussions

1223   indicates the location of the origin of the back trajectories. (b) Time-height

1224   representation of the individual back trajectories shown in the top panel.

1225

1226

(a)

(b)
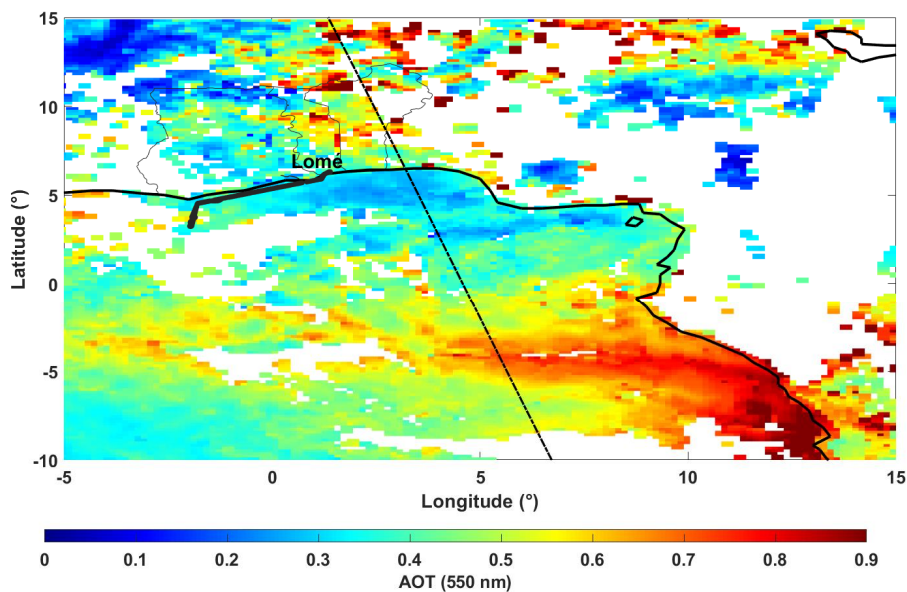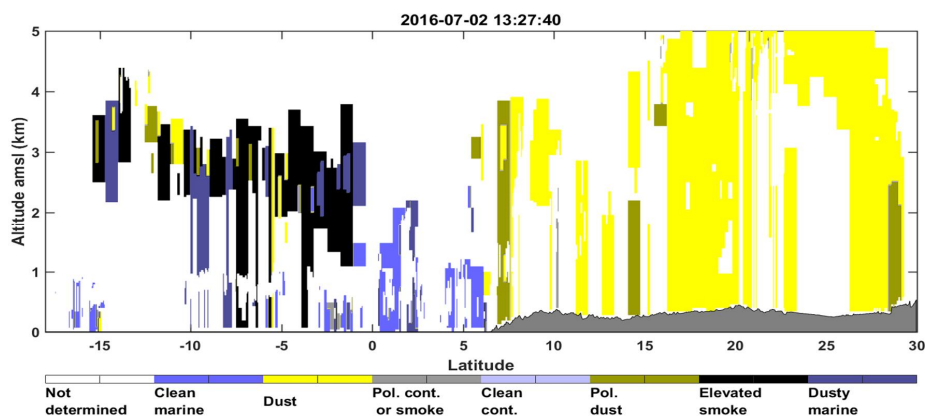
Figure 10: (a) Daily AOD obtained by averaging MODIS Dark target AOD (at 1325

UTC) and SEVIRI AOD (daily mean) on 2 July 2016. White areas indicate missing data.

Country borders of Ghana, Togo and Benin are shown as thin solid black lines. The

straight dashed-dotted line indicates the location of the CALIOP afternoon overpass

Atmospheric
Chemistry
and Physics
Discussions

1231   at 1327 UTC. The thick solid black line represents the ATR 42 flight track. (b) CALIOP-

1232   derived aerosol classification for the afternoon overpass.

1233

1234

(a)
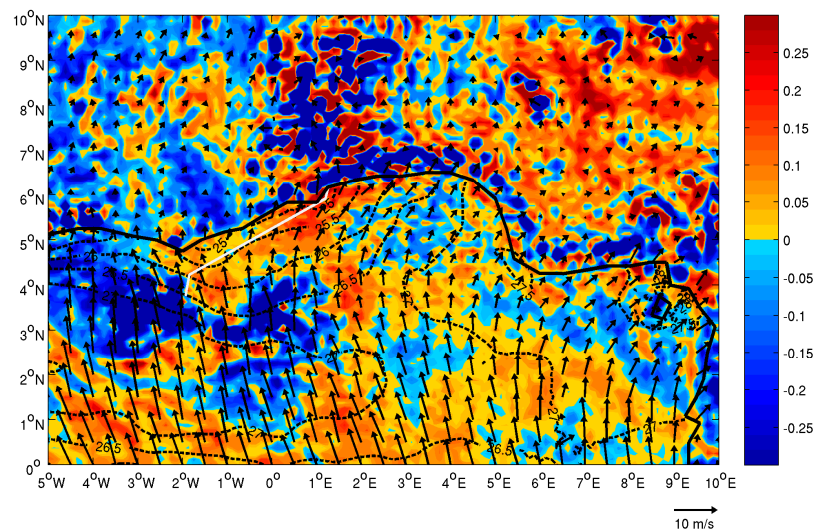
(b)
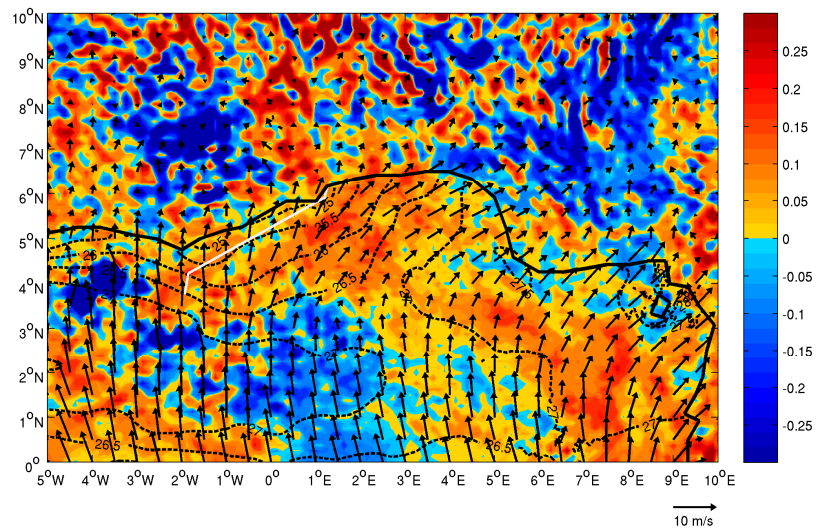
1235

1236   Figure 11: Vertical velocity averaged between 850 and 600 hPa (color, Pa s⁻¹) with

1237   10-m winds (vectors) and SST (contours, black dotted lines) from IFS analyses at (a)

1238   1200 UTC and (b) 1800 UTC. The thick black line represents the SWA coastline. The

1239   straight white line represents the ATR 42 flight track.

Atmospheric
Chemistry
and Physics
Discussions

1240

(a)

(b)

(c)
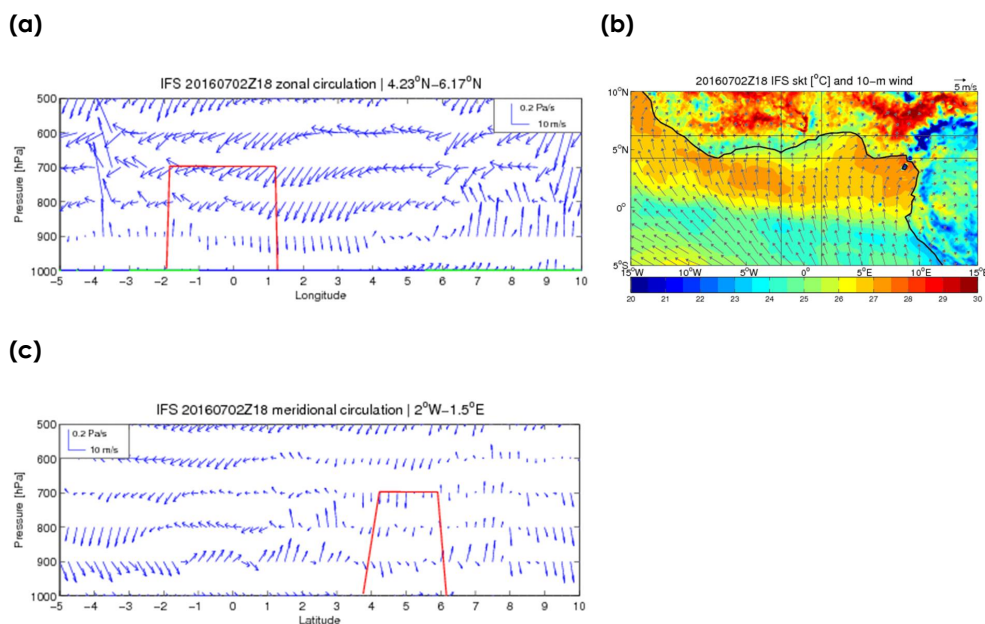
1241   Figure 12: (a) West–east oriented vertical cross section (1000–500 hPa) of zonal-

1242   vertical wind vectors from IFS analyses (blue) between 5°W and 10°E averaged

1243   between 4.54°N and 6.17°N at 1800 UTC on 2 July 2016. The thick red line is the

1244   projection of the ATR 42 aircraft track onto the cross-section. The thick green and

1245   blue lines at the bottom of the graph indicate the presence of land and ocean,

1246   respectively. Surface characteristics are defined based on the dominating surface

1247   type in the latitudinal band considered for the average of the wind field. (b) IFS skin

1248   temperature (colors) and wind field at 10 m (vectors) at 1800 UTC. The former,

1249   originally at 0.125° resolution, has been linearly interpolated onto the Copernicus grid

1250   at 5 km before computing the skin temperature differences between the

1251   observations and the model. (c) North-south oriented vertical cross section (1000–500

1252   hPa) of meridional-vertical wind vectors from IFS analyses (blue) between 5°S and

1253   10°N averaged between 2°W and 1.5°E at 1800 UTC. The thick red line is the

Atmospheric
Chemistry
and Physics
Discussions

1254   projection of the ATR 42 aircraft track onto the cross-section. Cross-sections shown in

1255   (a) and (c) are computed in the zonal and meridian windows delimited east-west

1256   and north-south lines, respectively, shown in (b).

1257

(a)   (b)
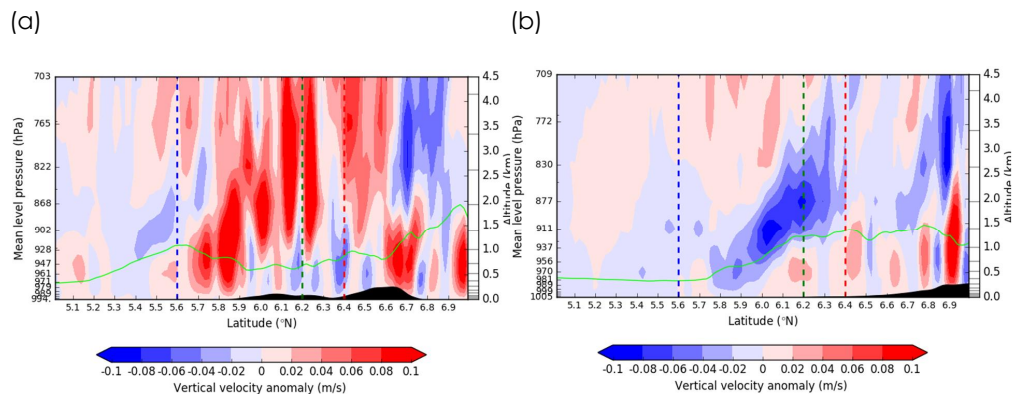
1258

Figure 13: Vertical velocity anomaly along (a) the western most transect shown in

Figure 1b (transect I) and (b) the eastern most transect shown in Figure 1b (transect

IV), from the WRF 2-km simulation. The anomalies are computed with respect to the

average vertical velocity between 1°W and 1°E.

1263